DOI: https://doi.org/10.2138/am-2020-7388. http://www.minsocam.org/

Revision 2

The composition of garnet in granite and pegmatite from the Gangdese orogen in southeastern Tibet: constraints on pegmatite petrogenesis

Meng Yu[1], Qiong-Xia Xia[1, 2 *], Yong-Fei Zheng[1, 2], Zi-Fu, Zhao, Yi-Xiang Chen[1, 2], Ren-Xu Chen[1, 2], Xu Luo[1], Wan-Cai Li[1, 2], Haijun Xu[3]

1. CAS Key Laboratory of Crust-Mantle Materials and Environments, School of Earth and Space Sciences, University of Science and Technology of China, Hefei 230026, China
2. CAS Center for Excellence in Comparative Planetology, Hefei 230026, China
3. State Key Laboratory of Geological Processes and Mineral Resources, Faculty of Earth Sciences, China University of Geosciences, Wuhan 430074, China

[*] Corresponding author. Email: qxxia@ustc.edu.cn

ABSTRACT

Two generations of garnet are recognized in a granite and a pegmatite from the Gangdese orogen in southeastern Tibet on the basis of a combined study of petrography, major and trace element profiles, and garnet O isotopes. Zircon U–Pb dating and Hf–O isotope compositions also help constrain the origin of both granite and pegmatite. The first generation of garnet (Grt-I) occurs as residues in the center of garnet grains, and it represents an early stage of nucleation related to magmatic–hydrothermal fluids. Grt-I is dark in BSE images, rich in spessartine, and poor in almandine and grossular. Its chondrite-normalized REE patterns show obvious negative Eu anomalies and depletion in HREE relative to MREE. The second generation of pegmatite garnet (Grt-II) occurs as the rim of euhedral garnets or as patches in Grt-I domains of the pegmatite, and it crystallized after dissolution of the preexisting pegmatite garnet in the presence of the granitic magma. Compared with Grt-I domains, Grt-II is bright in BSE images, poor in spessartine, and rich in almandine and grossular contents. Its chondrite-normalized REE patterns exhibit obvious negative Eu anomalies but enrichment in HREE relative to MREE. The elevated grossular and HREE contents for Grt-II relative to Grt-I domains indicate that the granitic magma had higher contents of Ca than the magmatic–hydrothermal fluids. The garnets in the granite, from core to rim, display homogenous profiles in their spessartine, almandine, and pyrope contents but increasing grossular and decreasing REE contents, and they are typical of magmatic garnets that crystallized from the granitic magma. Ti-in-zircon temperatures demonstrate that the granite and pegmatite may share the similar temperatures for their crystallization. Grt-II domains in the pegmatite have the same major and trace element compositions as the garnets in the granite, suggesting that the pegmatite Grt-II domains crystallized from the same granitic magma. Therefore, the pegmatite crystallized at first from early magmatic–hydrothermal fluids, producing small amounts of Grt-I, and the fluids were then mixed with the surrounding granitic magma. The U–Pb dating and Hf–O isotope analyses of zircons from the granite and pegmatite yield almost the same U–Pb ages of 77–79 Ma, positive $\varepsilon_{Hf}(t)$ values of 5.6 to 11.9, and $\delta^{18}O$ values of 5.2‰ to 7.1‰. These data indicate that the granite and pegmatite were both derived from reworking of the juvenile crust in the newly accreted continental margin prior to the continental collision in the Cenozoic.

Keywords: hydrothermal garnet; magmatic garnet; pegmatite; dissolution–reprecipitation

INTRODUCTION

Garnet is common in metamorphic rocks, and it is useful for assessing metamorphic conditions. Due to its stability over a wide range of temperatures and pressures, it is found widely in a remarkably diverse range of tectonic settings and rock types (e.g., Baxter and Scherer, 2013). Although garnet is less frequently present in magmatic rocks, it is common in S-type granites (e.g., Steven et al., 2007; Erdmann et al., 2009; Villaros et al., 2009; Lackey et al., 2012; Melo et al., 2017). Similar to metamorphic garnet, the composition of magmatic garnet is also useful for constraining the origin of host granites (e.g., Dahlquist et al., 2007; Steven et al., 2007; Villaros et al., 2009). It is therefore essential to determine the origin of garnet in a granite in order to understand the petrogenesis of the rock. Several different origins have been proposed for garnet in granites: (1) phenocrysts crystallized from magmatic melts (Dahlquist et al., 2007; Narduzzi et al., 2017), (2) xenocrysts derived from crustal rocks (Kawabata and Takafuji, 2005), (3) peritectic growth from incongruent melting (Stevens et al., 2007; Dorais et al., 2009; Xia et al., 2016), and (4) precipitation from hydrothermal fluids (Gasper et al., 2008; Dziggel et al., 2009).

There are also many reported examples of garnet in aplites and pegmatites (Arredondo et al., 2001; Gadas et al., 2013; Samadi et al., 2014a, b), which is generally considered magmatic in origin (Manning, 1983; Deer et al., 1992; Muller et al., 2012). In most cases, however, zoning of major and trace elements in the garnets of aplites and pegmatites differs from those in the other magmatic garnets (e.g., Samadi et al., 2014a, b), implying possibly different origins. Pegmatites have long been viewed as essentially igneous rocks because of their bulk compositions. The origins of pegmatites, however, is still controversial on some fronts such as textures and trace elements (London and Kontak, 2012). It is commonly accepted that most pegmatites crystallized from residual melts after the crystallization of granitic magmas, but some pegmatites may form as a result of protracted fractional crystallization and crustal anatexis (Simmons and Webber, 2008). Because the composition of garnet is very sensitive to changes in temperature and pressure, a study of its features may provide insights into pegmatite petrogenesis.

Numerous garnet-bearing pegmatite veins occur in granite bodies in the Gangdese orogen in southeastern Tibet (Fig. 1). To understand the origin of these pegmatite veins and their relationship to the granite bodies, we have made EPMA, LA–ICP–MS and SIMS analyses to establish the major and trace element zoning patterns of garnets and to determine the O isotope compositions of garnet and zircon grains from the pegmatites and associated granites. The results provide new constraints on the origin of both types of rock as well as their petrogenetic relationships.

GEOLOGICAL SETTING AND SAMPLES

The Himalayan-Tibetan plateau is composed mainly of four E–W-trending orogens or terranes (Fig. 1a), which from south to north are the Himalayan orogen, Lhasa terrane, Qiangtang orogen and Songpan–Ganzi terrane. It is not produced by a simple episode of continental collision in the Cenozoic as originally thought. Instead, it consists of composite orogens that were generated not only by accretionary orogenies from the Early Paleozoic through the Late Paleozoic to the Mesozoic but also by collisional orogeny in the Cenozoic (Zheng et al. 2013, 2019). The Lhasa terrane is separated from the Himalayan orogen to the south by the Indus–Yarlung suture zone, and from the Qiangtang orogen to the north by the Bangong–Nujiang suture zone (Yin and Harrison, 2000). The Lhasa terrane is a huge tectonic–magmatic unit approximately 100–300 km wide and 2500 km long (Dewey et al., 1988; Pearce and Deng, 1988), and it is composed of Mesozoic to Cenozoic igneous rocks, Paleozoic–Mesozoic sedimentary rocks, and a Precambrian metamorphic basement (e.g., Xu et al., 1985; Dewey et al., 1988; Harris et al., 1988a; Yin and Harrison, 2000; Pan et al., 2006; Dong et al., 2014). Based on the distribution of different sedimentary rocks and ophiolites (Pan et al., 2006; Zhu et al., 2011; Pan et al., 2012), the Lhasa terrane is subdivided into the northern, central, and southern subterranes that are separated by the Shiquan River–Nam Tso Mélange Zone (SNMZ) and the Luobadui–Milashan Fault (LMF), respectively (Fig. 1b).

<Figure 1>

The southern margin of Asian continent was subducted by the Neo-Tethyan oceanic slab in the Mesozoic, giving rise to continental arc magmatism for accretionary orogeny to form the Gangdese orogen in the Lhasa terrane (Zheng et al., 2013). Then the Gangdese continental arc llithosphere was subducted by the Indian continental lithosphere in the Early Cenozoic, leading to collisional orogeny for the formation of the Himalayan orogen (Zheng and Wu, 2018). The Gangdese orogen is a huge belt of plutonic rocks in the southern and central parts of the Lhasa terranes (Searle et al., 1987). It is the largest individual batholith in the Himalayan-Tibetan magmatic belt, extending from the Kailas in the west to Namche Barwa in the east, and it is made up mainly of diorites, granodiorites and granites with emplacement ages lasting from 198 to 43 Ma (e.g., Debon et al., 1986; Harris et al., 1990; Chung et al., 2003, 2005, 2009; Chu et al., 2006; Wen, 2007; Wen et al., 2008a, b; Ji et al., 2009, 2014; Ravikant et al., 2009). Numerous studies of the Gangdese intermediate to felsic intrusive rocks in the southern Gangdese area indicate a magmatic "flare-up" at ca. 100–80 Ma in the early phase of Late Cretaceous (Harris et al., 1988a, b; Chung et al., 2005; Chu et al., 2006; Mo et al., 2007; Wen et al., 2008a, b; Ji et al., 2009; Zhu et al., 2011, 2012; Ma et al., 2013a, b, c). Furthermore, three stages of magmatism at 95–86, 85–73, and 68–60 Ma during the Late Cretaceous to early Paleocene have been identified in the Gangdese orogen along the northern margin of the southern Lhasa subterrane (Wen et al., 2008a, b; Ji et al., 2014; Tang et al., 2019). The last stage of felsic magmatism is delayed to the continental collision at 55±10 Ma (Zheng and Wu, 2018).

The present study focuses on Late Cretaceous felsic plutons and pegmatitic veins at Langxian in the southeastern margin of the Gangdese orogen (Fig. 1b). These plutons were intruded into Late Paleozoic metamafic to metafelsic rocks that crop out close to the Langxian area (Wang et al., 2013). Two samples were collected from the Langxian pluton (Fig. 1), which consists mainly of medium-grained granitoids (granite 12LS257) with minor felsic or pegmatite veins (pegmatite 12LS258) (Fig. 2). There are clear contact boundaries between pegmatites and granites, and the pegmatite is included within and cut by the granite (Fig. 2a). The mineral assemblages of the pegmatite and granite are similar, with quartz, K-feldspar, plagioclase, and muscovite as the major minerals, and biotite, garnet, zircon, and apatite as the common accessory minerals (Fig. 3). Garnet grains in the pegmatite are conspicuous in the field and about 1 mm in size (Fig. 2b and c), and under a microscope they can be described as phenocrysts (Fig. 3d–f). In contrast, the garnets in granite 12LS257 are not visible in the field, even in thin-section, but were separated using heavy liquid methods.

The mineral abbreviations used in this paper are from Whitney and Evans (2010). For trace elements we follow the conventional terminology of light rare earth elements (LREE), heavy rare earth elements (HREE), and high field strength elements (HFSE).

<Figures 2 and 3>

ANALYTICAL METHODS

Whole-rock major and trace elements

Major and trace elements of whole-rock samples were analyzed at the ALS laboratory

Group in Guangzhou, China. Sample powders were mixed with either lithium borate or lithium metaborate flux and fused in a furnace at ~1000 °C. Flat glass discs were prepared from the melt and analyzed by X-ray fluorescence spectrometry for major elements. Trace-element analysis was performed by inductively coupled plasma–mass spectrometry (ICP–MS) on solutions after flat glass has been completely dissolved in 4% nitric acid. The repeated analyses of the standards GSR-2 and GSR-3 indicate that analytical uncertainties are better than ±1–2% for major elements and better than ±5% for most trace elements. Major- and trace- element compositions of granite and pegmatite are presented in the appendix Table S1.

Mineral major and trace elements

Mineral separates were extracted by crushing, sieving and heavy liquid methods, and then purified by hand picking under a binocular microscope. Zircon and garnet were mounted in epoxy resin and then polished down to expose the grain centers. Transparent zircon grains with few cracks were selected for O and Hf isotopes, U–Pb dating, and trace element analysis. Some garnets were selected for major and trace element analyses.

Mineral inclusions in garnet and zircon were carefully examined in thin section under a microscope and by the Laser Raman before major and trace element analyses. The laser Raman analysis of mineral inclusions was made on a Jobin Yvon LabRAM HR Evolution micro-Raman spectrometer, equipped with a confocal optics, Air-cooled CCD detector and a 532 nm Ar laser excitation source at CAS Key Laboratory of Crust-Mantle Materials and Environments (CAS-KL-CMME) in University of Science and Technology of China (USTC), Hefei. The beam size for Raman spectroscopy was ~1 μm. Monocrystalline silicon and polystyrene were analyzed during the analytical session to monitor the precision and accuracy of the Raman data.

Major element mapping of garnet was undertaken by the energy dispersive spectrometry (EDS) on Oxford Inca X-Max 50 and the scanning electron microscope (SEM) on Fei Quanta 450 FEG at State Key Laboratory of Geological Processes and Mineral Resources in China University of Geosciences, Wuhan. The measurements were carried out with an accelerating voltage of 20 kV, a spot size of 6.0 μm and a working distance of 12 mm.

Major element analyses of garnet were made on a Shimadzu EPMA-1600 electron microprobe (EMP) at CAS-KL-CMME in USTC, Hefei, China. The working conditions were set at 15 kV of accelerating voltage and a beam current of 2×10^{-8} A, with a beam size of 1 μm. Homogenously synthetic oxides and well-characterized natural minerals from SPI Supplies

Standards were used as standards. The procedures of standard correction on the three components of matrix effects, including atomic number (Z), absorption (A) and fluorescence (F), commonly called the ZAF correction, were used for data reduction. The precision for most major elements (e.g., atomic numbers are greater than 10 and concentrations are higher than 10%) are better than ±2 % (1σ).

Major and trace elements in garnet were also simultaneously analyzed utilizing a laser ablation-inductively coupled plasma mass spectrometer (LA-ICPMS) at CAS-KL-CMME in USTC, Hefei. This was made on the same garnet grains as the EMP analysis, and BSE images were used to efficiently avoid cracks and mineral inclusions. Detailed operating conditions for the laser ablation system and the ICP-MS instrument and data reduction are the same as descriptions by Liu et al. (2008). Laser sampling was performed using a GeoLas HD laser with a diameter of 32 μm for zircon and 24 μm for garnet. The laser frequency was 6 Hz and the energy density was 7 $J·cm^{-2}$, and a laser depth was ~10 μm. An Agilent 7900 ICP-MS instrument was used to acquire ion-signal intensities. Helium was applied as a carrier gas. Argon was used as the make-up gas and mixed with the carrier gas via a T-connector before entering the ICP.

Each analysis incorporated a background acquisition of approximately 20 s (gas blank) followed by 50 s data acquisition from the sample. The Agilent Chemstation was utilized for the acquisition of each individual analysis. Off-line selection and integration of background and analyzed signals, and time-drift correction and quantitative calibration were performed by ICPMSDataCal (Liu et al., 2008, 2010a). Trace element concentrations were calibrated by using ^{29}Si as internal calibrant and NIST SRM610 as the reference material. The precision and accuracy of the NIST-610 analyses are ±2-5% for most elements at the ppm concentration level. Element contents were calibrated against multiple-reference materials (BCR-2G, BIR-1G and BHVO-2G) without applying internal standardization (Liu et al., 2008). The preferred values of element concentrations for the USGS reference glasses are from the GeoReM database (http://georem.mpch-mainz.gwdg.de/). Analyses of USGS rock standards (BCR-2G and BHVO-2G) indicate that the precision and accuracy (1σ) are better than ±10% for trace elements and rare earth elements, and ±2% for major elements. Limits of detection (LOD) for these USGS standards were described by Gao et al. (2002) in detail. LOD for each element and analysis were calculated individually as three times the standard deviation of the background signal (taken before ablation) divided by element sensitivity during the respective ablation. For non-significant analytical signals, LOD values are also reported (marked by < LOD). It has to be mentioned that the area and depth of laser ablation are much bigger than the volume sampled by the EMP analysis, thus the major elements analyzed by EMP and LA-ICPMS are not exactly the same, and the LA-ICPMS analysis may have a lower precision than the EMP analysis. Major element compositions analyzed by EMP were used in this study.

SIMS zircon in-situ oxygen isotopes

Firstly, catholuminescence (CL) images of zircons were obtained using a microprobe JEOL JXA-8900RL in Chinese Academy of Geological Sciences, Beijing, with imaging at 20 kV and 15 nA. Then the in-situ O isotopes in zircon were analyzed using a Cameca IMS 1280-HR at State Key Laboratory of Isotope Geochemistry in Guangzhou Institute of Geochemistry, Chinese Academy of Sciences (CAS), Guangzhou. Analytical procedures are the same as those described by Li et al. (2010a). The Cs^+ primary ion beam was accelerated at 10 kV, with an intensity of ca. 2 nA (Gaussian mode with a primary beam aperture of 200 μm to reduce aberrations) and rastered over a 10 μm area. The analysis spot was about 20 μm in diameter (10 μm beam diameter + 10 μm raster). Oxygen isotopes were measured in multi-collector mode using two off-axis Faraday cups. The NMR (Nuclear Magnetic Resonance) probe was used for magnetic field control with stability better than 2.5 ppm over 16 h on mass 17. One analysis takes ~3.5 min consisting of pre-sputtering (~30 s), 120 s of automatic tuning of the secondary beam, and 64 s of analysis. The instrumental mass fractionation (IMF) was corrected using in-house zircon standard Penglai with a recommended $\delta^{18}O$ value of 5.31±0.10‰ with reference to the Vienna standard mean oceanic water (VSMOW) that has a recommended $^{18}O/^{16}O$ ratio of 0.0020052 (Li et al., 2010b). The measured $^{18}O/^{16}O$ ratios for samples (raw data) were firstly normalized relative to the VSMOW, and then corrected for IMF (Li et al., 2010a).

The internal precision of a single analysis was generally better than ±0.20‰ (2σ standard error) for $\delta^{18}O$ values. The external precision, measured by the reproducibility of repeated analyses of the Penglai standard during three sessions of this study, is ±0.41‰ (2SD, n=38), ±0.34‰ (2SD, n = 34) and ±0.34‰ (2SD, n = 50). During the three sessions, a second zircon standard Qinghu was measured as an unknown to ascertain the veracity of the IMF. Three series of analyses in twenty, eighteen and twenty-six measurements, respectively, of Qinghu zircon standard yield a weighted mean of $\delta^{18}O$ = 5.51 ±0.30‰ (2SD), 5.51 ± 0.36‰ (2SD) and 5.53 ± 0.53‰ (2SD). These values are in good agreement within errors with a reported value of 5.4 ± 0.2‰ (Li et al., 2013). Zircon O isotope data are listed in Table 5.

Zircon U–Pb ages and trace elements

After the SIMS zircon O isotope analysis, zircon U–Pb dating and trace element analysis were simultaneously performed by the LA-ICPMS in-situ method at State Key Laboratory of Geological Processes and Mineral Resources in China University of Geosciences, Wuhan. Laser ablation sampling was performed using a Geolas 2005 system equipped with a 193 nm ArF-excimer laser. An Agilent 7500a ICP-MS was used to acquire ion-signal intensities. Detailed instrumental conditions and data acquisition were described by Liu et al. (2010b, 2010c) and Zong et al. (2010). For zircon trace element and U–Pb isotope analyses, the blank was very low because high purity argon and helium was used. The ICP-MS measurements were carried out by using time-resolved analysis and peak hopping at one point per mass and the dwell time for each isotope was set at 6 ms for Si, Ti, Nb, Ta, Zr and REE, 15 ms for ^{204}Pb, ^{206}Pb, ^{207}Pb and ^{208}Pb, and 10 ms for ^{232}Th and ^{238}U. Each spot analysis includes 20s of background acquisition and 40s sample data acquisition. Trace element concentrations were calibrated by using ^{29}Si as an internal calibrant and NIST SRM610 as a reference material. The precision and accuracy of NIST-610 analyses are ±2-5% for most elements at the ppm concentration level. Zircon Ti temperatures are calculated following the calibration of Watson et al. (2006).

The U–Pb isotope ratios such as ^{207}Pb/^{206}Pb, ^{206}Pb/^{238}U, ^{207}Pb/^{235}U and ^{208}Pb/^{232}Th ratios were calculated using Glitter 4.0 software (Macquarie University), which were then corrected using the zircon 91500 as an external calibrant with a ^{206}Pb/^{238}U age of 1065.4±0.6 Ma (Wiedenbeck et al., 1995). All the measured isotope ratios of zircon 91500 were regressed over the course of the analytical session and used to calculate correction factors. These correction factors were then applied to each sample in order to correct both instrumental mass bias and depth-dependent elemental and isotopic fractionation. Apparent and discordant U–Pb ages were calculated by the ISOPLOT program (Ludwig, 2003). The obtained U-Pb ages for zircon standards GJ-1 are consistent with the preferred values within about ±2% uncertainty (2σ) by simple external calibration against zircon standard 91500 (Liu et al., 2010b).

Zircon Lu-Hf isotopes

After the zircon O isotope analysis, U–Pb dating and trace element analysis, the in-situ measurement of zircon Lu-Hf isotopes was performed on a Neptune MC-ICPMS at State Key Laboratory of Geological Processes and Mineral Resources in China University of Geosciences, Wuhan. A "wire" signal smoothing device is included in this laser ablation system, by which smooth signals are produced even at very low laser repetition rates down to

1 Hz (Hu et al., 2012a). The energy density of laser ablation that was used in this study was 5.3 J cm^{-2}. Helium was used as the carrier gas within the ablation cell and was merged with argon (makeup gas) after the ablation cell. As demonstrated by our previous study, for the 193 nm laser a consistent 2-fold signal enhancement was achieved in helium than in argon gas (Hu et al., 2008a). We used a simple Y junction downstream from the sample cell to add small amounts of nitrogen (4 ml min^{-1}) to the argon makeup gas flow (Hu et al., 2008b). Compared to the standard arrangement, the addition of nitrogen in combination with the use of the newly designed X skimmer cone and Jet sample cone in Neptune Plus improved the signal intensity of Hf, Yb and Lu by a factor of 5.3, 4.0 and 2.4, respectively. All data were acquired on zircon in single spot ablation mode at a spot size of 44 μm in this study. Each measurement consisted of 20 s of acquisition of the background signal followed by 50 s of ablation signal acquisition. Detailed operating conditions for the laser ablation system and the MC-ICP-MS instrument and analytical method are the same as description by Hu et al. (2012b).

The major limitation to the accuracy of in-situ Hf isotope determination by LA-MC-ICP-MS is the very large isobaric interference from ^{176}Yb and, to a much lesser extent ^{176}Lu on ^{176}Hf. It is known that the mass fractionation of Yb (β_{Yb}) is not constant over time and that the β_{Yb} from the introduction of solutions is unsuitable for *in situ* zircon measurements (Woodhead et al., 2004). The under- or over-estimation of the β_{Yb} value would undoubtedly affect the accurate correction of ^{176}Yb and thus the determined $^{176}Hf/^{177}Hf$ ratio. We applied the directly obtained β_{Yb} value from the zircon sample itself in real-time in this study. The $^{179}Hf/^{177}Hf$ and $^{173}Yb/^{171}Yb$ ratios were used to calculate the mass bias of Hf (β_{Hf}) and Yb (β_{Yb}), which were normalised to $^{179}Hf/^{177}Hf$ =0.7325 (Segal et al., 2003) and $^{173}Yb/^{171}Yb$=1.132685 (Fisher et al., 2014) using an exponential correction for mass bias. Interference of ^{176}Yb on ^{176}Hf was corrected by measuring the interference-free ^{173}Yb isotope and using $^{176}Yb/^{173}Yb$ =0.79639 (Fisher et al., 2014) to calculate $^{176}Yb/^{177}Hf$. Similarly, the relatively minor interference of ^{176}Lu on ^{176}Hf was corrected by measuring the intensity of the interference-free ^{175}Lu isotope and using the recommended $^{176}Lu/^{175}Lu$ =0.02656 (Blichert-Toft et al., 1997) to calculate $^{176}Lu/^{177}Hf$. We used the mass bias of Yb (β_{Yb}) to calculate the mass fractionation of Lu because of their similar physicochemical properties. Off-line selection and integration of analyte signals, and mass bias calibrations were performed using ICPMSDataCal program (Liu et al., 2010b).

Oxygen isotopes in garnet and quartz grains

The O isotope analysis of mineral separates was carried out by laser fluorination technique using a 25W CO_2 laser MIR-10 at CAS-KL-CMME in USTC, Hefei. About 1.5 to 2.0 mg mineral separates reacted with BrF_5 at vacuum, and the obtained O_2 was directly transferred to a Delta+ mass spectrometer for the measurement of $^{18}O/^{16}O$ and $^{17}O/^{16}O$ ratios (Zheng et al., 2002). Oxygen isotope data were reported in the $\delta^{18}O$ notation relative to the VSMOW standard. Reproducibility for repeated measurements of each standard on a given day was better than ±0.1‰ (1σ) for $\delta^{18}O$. The National Standard of China GBW04416 quartz with $\delta^{18}O$ =11.1‰ was used as the reference material (Zheng et al., 1998). The results are listed in Table 5. Oxygen isotopic temperatures are calculated by differences in $\delta^{18}O$ values between quartz and other minerals in terms of theoretically calibrated fractionation factors by Zheng (1993), assuming preservation of isotope equilibration at the scale of sample measurement. The calculated temperature uncertainties are about at levels of ±30 to ±50ºC.

RESULTS

Garnet major elements

Five garnet grains from the two granite and pegmatite samples were selected for profile analyses by EMP and LA–ICP–MS, respectively. The garnets from both granite and pegmatite consist of spessartine–almandine solid solutions, with compositions of $Sps_{46–49}Alm_{40–43}Pyr_{4–5}Grs_{1–5}$ in the granite and $Sps_{48–60}Alm_{32–43}Pyr_{3–5}Grs_{0–3}$ in the pegmatite (Table 1). BSE images show that the garnets from the granite are almost homogeneous, whereas those from the pegmatite have obvious chemical zoning (Fig. 4). Major element X-ray mappings on the three garnet grains from the pegmatite show strong zoning with respect to Mn, Fe, and Ca, but weak zoning or no zoning with respect to Mg (Fig. 5). For instance, from center to rim, the concentrations of spessartine decrease from 58.7 to 48.2 mol.%, the concentrations of almandine increase from 33.7 to 42.5 mol.%, and for garnet grain 12LS258-G2 the grossular content increases from almost zero to 2.0 mol.% (Table 1; Fig. 4h–j). In contrast, the compositional profiles for garnets from the granite display almost flat patterns for almandine, spessartine, and pyrope, and two grains show only weak zoning in grossular (Fig. 4f and g).

<Figures 4 and 5>
<Table 1>

Garnet trace elements

Garnets from the granite show slight variations in their chondrite-normalized REE distributions (Fig. 4k and l). They all display flat MREE–HREE distributions in their centers, with $(Yb/Gd)_N$ values of 3.2 to 14 (Table 2). On the other hand, the rims show steeper MREE–HREE distributions, with $(Yb/Gd)_N$ values of 28 to 85. In general, the trace element profiles of garnets from the granite show obvious zoning with both compatible elements (e.g., Y, Dy, Sc, and V) and incompatible elements (e.g., Nd, Zr, and Nb) decreasing from centers to rims (Fig. 6a-b).

Similar to the major element profiles, three garnets from the pegmatite show evident variations in chondrite-normalized REE distributions and trace element profiles (Figs. 4 and 6). As illustrated in Fig. 4m–o, the inner domains (e.g., LA spots 1–4, 2–4, and 3–5) display almost flat MREE–HREE distributions, with $(Yb/Gd)_N$ values of 1.4 to 2.7 (Table 2). However, the outer rims are relatively enriched in HREE, with $(Yb/Gd)_N$ values of 3.7 to 24. In contrast, the in-between domains have the lowest HREE concentrations and display depleted MREE–HREE distributions with $(Yb/Gd)_N$ values of 0.2 to 2.1. In trace element profiles (Fig. 6c–e), the compatible elements (e.g., Y, Yb, and Dy) show oscillatory variations, with the highest concentrations in the centers or rims and the lowest concentrations in the in-between domains. But the incompatible elements (e.g., Sm and Zr) gradually decrease from centers to rims.

<Figure 6>

Zircon U–Pb ages and trace elements

Zircons from the granite are light yellow, translucent, short to long prisms with lengths of 100 to 200 μm. They are euhedral and display core–rim structures (Fig. 7a). CL images show that most grains have bright rounded cores with obscure oscillatory or planar zoning and dark rims with clear oscillatory zoning. Some grains with dark CL images are euhedral crystals with regular oscillatory zoning. Raman analysis of these zircon grains indicated the presence of many inclusions of minerals such as apatite, quartz, and feldspar. Seven analyses on the bright cores of zircons from the granite yield variable U–Pb ages from 133 to 363 Ma (Fig. 7b) and relatively low Th/U ratios of 0.10 to 0.31 (Table 3). Their chondrite-normalized REE patterns show a characteristic feature of magmatic zircon (Fig. 7d), with positive Ce anomalies (Ce/Ce* = 3.8–16.3), negative Eu anomalies (Eu/Eu* = 0.02–0.33), and steep MREE–HREE patterns and $(Yb/Gd)_N$ values of 22.4 to 68.1 (Table 4). On the other hand, 26 analyses of black rims or single grains give consistent U–Pb ages of 76.1–80.5 Ma (Fig. 7b), yielding a weighted mean of 79.1 ± 0.5 Ma (Fig. 7c). These analyses give Th and U contents that vary markedly from 58.1 to 4987 ppm and 267 to 6615 ppm, respectively. Correspondingly, they have highly variable Th/U ratios of 0.04 to 1.11 (Table 3). Their chondrite-normalized REE patterns also show a characteristic features of magmatic zircon (Fig. 7d), with positive Ce anomalies (Ce/Ce* = 3.6–502), negative Eu anomalies (Eu/Eu* = 0.03–0.49), and steep MREE–HREE patterns and $(Yb/Gd)_N$ values of 14.9 to 78.0 (Table 4). Except for three analyses showing exceptionally high Ti contents of 22.6–25.7 ppm, the remaining Ti contents vary from 1.84 to 12.4 ppm, yielding Ti-in-zircon temperatures of 611 to 760 °C with a mean of 677 ± 37 °C (Table 4).

Zircons from the pegmatite are anhedral, murky-brown, and translucent, have a very weak CL brightness, and are unzoned or have a spongy texture (Fig. 7e). Raman analyses show that these zircons contain many inclusions of minerals such as quartz, apatite, biotite, and thorite. U–Pb dating of 14 grains yields consistent ages of 76.0–78.3 Ma, with a weighted mean of 76.8 ± 0.4 Ma (Fig. 7g). These zircons have exceptionally high U contents of 17,272–52,154 ppm and moderately high Th contents of 360–1691 ppm, leading to very low Th/U ratios of 0.02–0.03. Raman spectra obtained from the zircon domains with high Th–U contents show sharp peaks on the main bands, similar to those for the zircon domains with low Th–U contents from the granite. The apparent $^{206}Pb/^{238}U$ ages of ~77 Ma obtained for domains with high Th–U contents are indistinguishable from each other (Fig. 7d and f). Therefore, the effect of metamictization on zircon U-Pb ages is negligible.

The chondrite-normalized REE patterns (Fig. 7h) show positive Ce anomalies (Ce/Ce* = 1.1–90.9), negative Eu anomalies (Eu/Eu* = 0.04–0.33), flat MREE–HREE distributions, and $(Yb/Gd)_N$ values of 0.6 to 5.2 (Table 4). Except for three analyses with exceptionally high Ti values of 21.8–119 ppm, the remaining Ti contents of these zircons vary widely from 0.56 to 9.7 ppm, yielding a wide range of Ti-in-zircon temperatures of 538 to 738 °C with a mean of 634 ± 65 °C (Table 4).

<Figure 7 >

Zircon Lu–Hf isotopes

As shown in Fig. 8, the residual cores of magmatic zircon with the U–Pb ages of 133 to 363 Ma from the granite have low $^{176}Lu/^{177}Hf$ ratios of 0.000821 to 0.002019 and $^{176}Hf/^{177}Hf$ ratios of 0.282365 to 0.282470 (Table 5); their initial Hf isotope ratios vary from 0.282339 to 0.282447, yielding $\varepsilon_{Hf}(t)$ values of –11.7 to –3.5 and two-stage Hf model (T_{DM2}) ages of 1595 to 1932 Ma. In contrast, the newly grown domains of zircon at ~79 Ma from the granite have relatively high $^{176}Lu/^{177}Hf$ ratios of 0.001044 to 0.003875 and high $^{176}Hf/^{177}Hf$ ratios of 0.282884 to 0.283107; their initial Hf isotope ratios are evidently higher than those of the residual cores, yielding positive $\varepsilon_{Hf}(t)$ values of 5.6 to 11.9 and single-stage Hf model ages of 221 to 538 Ma with a peak at ~350 Ma (Fig. 8c).

In contrast, zircons from the pegmatite have the lowest $^{176}Lu/^{177}Hf$ ratios of 0.00014 to 0.000617, except for a very high value of 0.005564 in analysis #16. Nevertheless, these zircons have relatively high and homogeneous $^{176}Hf/^{177}Hf$ ratios of 0.282980 to 0.283026 and their initial Hf isotope ratios give positive $\varepsilon_{Hf}(t)$ values of 9.0 to 10.4, similar to those of the newly grown domains of zircon from the granite. The corresponding single-stage Hf model ages are 341 to 365 Ma, with a peak at ~356 Ma (Fig. 8d).

<Figure 8>

Oxygen isotopes in zircon, garnet, and quartz

Thirty-two spots were selected for the *in situ* O isotope analysis on zircons from the granite. All these domains have concordant U–Pb ages. The results show that the residual cores and overgrown rims of zircons from the granite have distinct $\delta^{18}O$ values, varying from 8.62 to 9.78‰ with an average of 8.45±1.48‰ for the cores and 6.06 to 7.05‰ with an average of 6.43 ± 0.13‰ for the rims (Fig. 8b). The residual cores are higher the overgrown rims in their $\delta^{18}O$ values, and both are higher than the normal mantle values of 5.3 ± 0.3‰ (Valley et al., 1998).

The garnet and quartz separates from the granite gave $\delta^{18}O$ values of 6.06‰ and 9.73‰, respectively. The O isotope fractionation between quartz and garnet yields a temperature of 657 °C, and the fractionation between quartz and the zircon rims gives a temperature of 708 °C (Table 5).

Fifteen *in situ* O isotope analyses on zircons from the pegmatite yield homogeneous $\delta^{18}O$ values of 5.19 to 6.00‰, with an average of 5.68 ± 0.27‰. This value is very close to the $\delta^{18}O$ values of 5.99‰ for garnet separates. Quartz from the pegmatite has a $\delta^{18}O$ value of 9.74‰. The O isotopic fractionation between quartz and garnet gives a temperature of 645 °C, and that between quartz and zircon yields a temperature of 597 °C.

DISCUSSION

Major element zoning in garnets

Garnet is highly refractory and can be stable over a wide rang of pressure and temperature (e.g., Kohn, 2003; Caddick and Kohn, 2013; Baxter et al, 2017). It usually displays a progressive decrease from core to rim in the spessartine component (called bell-shaped zoning) during prograde metamorphism (e.g., Hollister, 1966), although the zoning is always much more complex if the garnet grew during multiple stages of metamorphism (e.g., Kohn et al., 1997). This is due to the Rayleigh fractionation effect of Mn incorporation in garnet. In contrast, magmatic garnets in igneous rocks are characterized by homogeneous compositions, or even inverse bell-shaped zoning of the spessartine component, with Fe-rich and Mn-poor cores (e.g., Miller and Stoddard, 1981; du Bray, 1988; Dahlquist et al., 2007).

Pressure, temperature and the matrix compositions are three important variables affecting the garnet compositions (Baxter et al, 2017). As the granite and pegmatite were emplaced into the Gangdese batholith at a short time of ~77-79 Ma, they may have shared the same pressure. The Ti-in-zircon thermometry can be used to constrain the crystallization temperature of magmatic rocks (Watson et al., 2006). The LA-ICPMS analysis of zircons from the granite and pegmatite yields the variable Ti contents from 1.84 to 12.4 ppm and 0.56 to 9.7 ppm, respectively (Table 4). These correspond to Ti-in-zircon temperatures of 611 to 760 °C (mean 677 ± 37 °C) and 538 to 738 °C (mean 634 ± 65 °C), respectively. Thus the granite and pegmatite may share the similar pressure and temperature for their crystallization. In this regard, the garnet compositions are mainly controlled by the melt compositions from which they crystallized (du Bray, 1988).

It has been suggested that granitic magmas and pegmatite-forming melts differ significantly with regard to their dissolved H_2O contents and viscosities at comparable temperatures and pressures (Thomas and Davidson, 2012), and that these differences have a major influence on their element partitioning. Usually, hydrous felsic melts for pegmatite crystallization are of low viscosity and extremely evolved, exhibiting the melt–fluid immiscibility. Miller and Stoddard (1981) and Abbott (1981) argued that Mn/(Fe + Mg) ratios for magmatic garnet increase with melt differentiation and that Mn-rich garnets are probably precipitated from evolved Mn-rich melts. Moretz et al. (2013) also showed that garnet from the least evolved melt has the lowest MnO, MgO and CaO contents but the highest FeO content. Thus, magmatic garnets in less evolved granitoids are commonly Fe^{2+}-rich, whereas garnets in highly evolved granitic aplites and pegmatites commonly have higher Mn contents (Fig. 9) (e.g., Baldwin and Von Knorring, 1983; du Bray, 1988; Whitworth, 1992; Arredondo et al., 2001; Samadi et al., 2004a; London, 2008; Muller et al., 2012). Our specimens of garnet from both granite and pegmatite have high MnO contents of ~20–25 wt.% (Table 1). This demonstrates that the granite and pegmatite are likely highly evolved products of the same granitic melt.

Garnets from the granite display almost homogeneous compositions except Ca (Fig. 4f and g), which is typical of magmatic garnets in granitoid batholiths (Aydar and Gourgaud, 2002; Mirnejad et al., 2008). However, the major element profiles for garnets from the pegmatite show a systematic decrease in spessartine but increase in almandine from centers to rims (Fig. 4h–j). This kind of center-to-rim decrease profile for spessartine has also been reported for pegmatite garnets from other localities (e.g., Manning, 1983; Whitworth, 1992; Thöni et al., 2003; Gadas et al., 2013; Samadi et al., 2014a), and has been explained by the compatible property of Mn in garnet. In a pegmatite-forming melt, garnet is the only phase that incorporates Mn. The precipitation and growth of garnet would lead to depletion of Mn relative to Fe in the melt and to a progressive change in the composition of garnet from Mn-rich (core) to Fe-rich (rim). Nevertheless, the compositions of garnet rims in the pegmatite are almost identical to those of garnets in the granite, implying that the granitic melts were compositionally similar to the pegmatite-forming melt from which the garnet rims crystallized.

Oscillatory zoning in the pegmatite garnet is defined by variations in grossular composition (Figs. 4h–j and 5). The decoupling between the Ca zoning and the Mn or Fe zoning may be related to the lower diffusion rate of Ca (Ganguly et al., 1998). For this reason, the grossular zoning in our garnet samples is more likely to represent the growth zoning profile than the zoning of other major components. Oscillatory zoning of major elements has often been reported for garnets in dacite and pegmatite (e.g., Thoni and Miller; 2004; Kawabata and Takafuji, 2005), and the repeated increases and decreases in elemental concentrations have been interpreted variously as due to (1) cyclic changes in pressure, temperature, fluid pressure, or fluid composition (e.g., García–Casco et al., 2002; Dziggel et al., 2009); (2) changes in the garnet-producing reactions (e.g., Jamtveit and Anderson, 1992); or (3) rapid, cyclic growth of the garnet (Kohn, 2004). X-ray mapping of three grains of the pegmatite garnet shows that the low-Ca and high-Mn domains form irregular shapes within the mantles of the garnet phenocrysts, whereas the highest-Ca and lowest-Mn concentrations occur in the rims or in some centers (Fig. 5). As the major element concentrations in the centers and rims are almost identical, it is possible that the original centers were dissolved and replaced by new growths of garnet at the same time as the rims formed. This kind of garnet resorption and regrowth were also reported in atoll-shaped garnets in ultrahigh-pressure (UHP) eclogites from the Dabie orogen (Cheng et al., 2007). Many voids or pores are visible within the low-Ca domains (Grt-I), which may represent the passage of magmatic–hydrothermal fluids or volatiles during garnet growth (Geisler et al., 2003; Rubatto et al., 2008). Therefore, the domains of Grt-I were precipitated during an early stage of magmatic–hydrothermal fluid activity, whereas the high-Ca rims (Grt-II) were formed later from a second episode of fluids or melts, at which time some of the early Grt-I was replaced by Grt-II.

Trace element zoning in garnets

Trace element zoning in garnet is a tracer for the history of host metamorphic rocks, plutons, or batholiths (e.g., Spear and Kohn, 1996; Otamendi et al., 2002; Zhou et al., 2011; Xia et al., 2016). In many cases, trace elements provide a relatively complete history of the host rock, and this is because trivalent trace elements, especially the MREE and HREE, have large ionic radii and are thus relatively resistant to diffusion and metamorphic resetting (e.g., Hickmott and Spear, 1992; Gaspar et al., 2008; Konrad–Schmolke et al., 2008a, b). In contrast, major element zoning produced during garnet growth is often partially or completely homogenized at temperatures >680 °C after a period of time due to intracrystalline diffusion of divalent cations (Carlson and Schwarze, 1997; Carlson, 2002; Caddick et al., 2010; Cheng et al., 2020). As illustrated in Fig. 4, garnets from the granite have almost homogeneous compositions of several major elements such as Mn, Fe, and Mg, but with exception of Ca. However, their trace element profiles show a progressive zoning from core to rim with decreasing amounts of REE (Sm and Dy), Y and Zr (Fig. 6a-b), which can be well explained by the Rayleigh fractionation during garnet crystallization with cooling (Otamendi et al., 2002). However, the contents of Yb show irregular variations distinct from those of Y, which is very unusual and remains unknown. In garnet grains G1 and G2 from the granite, MREE contents display an obvious decrease relative to HREE, producing steeper MREE–HREE distribution patterns in the rims (Fig. 4k and l). This may be related to the preferential incorporation of HREE relative to MREE, which is consistent with the compatibility of REE within garnet (Draper et al., 2003).

The major element and some incompatible trace element profiles (such as for Nd, Zr, and Nb) for the pegmatite garnets show progressive variations from core to rim, but the compatible trace element profiles (such as for Dy, Yb, and Y) display oscillations (Fig. 6c-e).

The two episodes of garnet growth recorded by Ca zoning (Fig. 4) point to two episodes of magmatic or hydrothermal activity during the garnet growth, and this is confirmed by the positive correlations between concentrations of Y (Yb) and CaO (Fig. 10). The centers of the pegmatite garnets (e.g., LA spots 1–4C, 2–4C, and 3–5C) have flat to declining MREE–HREE distribution patterns (Fig. 4m–o), identical to the distributions in the centers of garnet from the granite (Fig. 4k-l). The trace element concentrations in the pegmatite garnet centers and outer-rims have concentrations comparable to those in the centers of garnets from the granite (Table 2; Fig. 6), suggesting that the pegmatite Grt-II domains were precipitated from the same granitic melts as the granite garnets. In contrast, the pegmatite Grt-I domains have the lowest Ca and HREE contents and depleted MREE–HREE patterns, thus confirming that the Grt-I and Grt-II domains have distinct sources. Depleted MREE–HREE distributions are usually observed in garnets related to hydrothermal fluids (e.g., Smith et al, 2004; Gasper et al., 2008; Dziggel et al., 2009). Therefore, the pegmatite Grt-I domains were precipitated from magmatic–hydrothermal fluids.

It has been reported that the incorporation of REE into garnet is strongly controlled by the major element compositions of the garnet (Gasper et al., 2008; Dziggel et al., 2009). For example, grossular-rich garnet tends to be more enriched in HREE, whereas andradite-rich garnet typically exhibits less HREE-enriched patterns (Dziggel et al., 2009). Our LA–ICP–MS analyses show that the HREE concentrations in the pegmatite garnets increase with CaO contents (Fig. 10), suggesting an increase of Ca in the second episode of fluids or melts. But the question then is posed: what is the reason for these elevated Ca contents? Positive correlations between Yb (Y) and CaO are often found in hydrothermal garnets from altered calc-silicate rocks (Gasper et al., 2008; Dziggel et al., 2009). However, in our studying area there are no carbonate rocks exposed near the outcrops of both granite and pegmatite, nor are there any carbonate inclusions in the garnets or the other minerals. Therefore, the high-Ca fluids or melts could not have been produced by the dissolution of local carbonate-rich rocks.

Whole-rock analyses of our granite and pegmatite samples show no Eu anomalies (Eu/Eu* = 1.10 and 1.00, respectively) in the chondrite-normalized REE distribution patterns (Appendix Fig. 1a). However, the negative Eu anomalies are prominent in the garnets from both granite and pegmatite (Fig. 4k–o), indicating that plagioclase had crystallized from the granitic magma and pegmatite-forming melts before the garnet growth. Both garnet and plagioclase are the two major Ca-rich phases in the granite and pegmatite. In a closed system, the early crystallization of plagioclase would decrease the Ca concentrations in the melt, leading to a decrease in the Ca content of garnet crystallized from the residual melt. However, this is contrary to the observation that our studied garnets from both granite and pegmatite display an increase in Ca at the rims (Fig. 4f–j). Thus, the early crystallization of plagioclase cannot explain the elevated Ca concentrations in the garnet rims. However, the comparably high major and trace element compositions of Grt-II domains in the pegmatite and garnet centers in the granite suggest that Grt-II domains in the pegmatite are related in some way to the magmatic garnet of the granite. In other words, the elevated Ca concentrations of Grt-II domains in the pegmatite are related to the granitic magma.

The trace element zoning in the pegmatite garnets demonstrates that Grt-I domains were precipitated from a magmatic–hydrothermal fluid whereas Grt-II domains in the pegmatite and the magmatic garnet in the granite crystallized from the granitic magma. As a consequence of the infiltration of the pegmatite by the granitic melt, some of Grt-I domains were dissolved and replaced by Grt-II, and the remnants of Grt-I domains were overgrown by rims of Grt-II. The results of these processes are shown by the patchy Grt-I domains in Fig. 5, and the oscillatory zoning of major and trace elements in the pegmatite garnets (Fig. 6). The decoupling of Ca and the compatible elements (Y and HREEs) between Grt-I and Grt-II domains (Fig. 10) also support that the pegmatites could not crystallize from the residual melts after the crystallization of the granitic magma. Otherwise, the crystallization of phases (quartz and plagioclase) poor in Fe, Mg, and Mn would drive the residual melts to the progressive enrichment in these elements as well as Y and HREE. Thus it is also reasonable to infer that the pegmatite was formed earlier than the granite, consistent with the inclusion of the pegmatite within the granite (Fig. 2a).

IMPLICATIONS FOR THE ORIGIN OF BOTH GRANITE AND PEGMATITE

The use of zircon Hf isotopes to trace the origins of igneous rocks and the evolution of crust and mantle over time is now well established (e.g., Amelin et al., 1999, 2000; Griffin et al., 2000, 2002; Andersen et al., 2002; Samson et al., 2003; Zheng et al., 2006, 2009). It also demonstrated that magmatic zircon is capable of preserving their igneous $\delta^{18}O$ values through subsolidus hydrothermal alteration and granulite-facies metamorphism (Valley, 2003; Zheng et al., 2004). In other words, zircon O isotopes can also be used to trace the composition of magmatic sources with little influence from closed-system metamorphic and magmatic processes (Chen et al., 2015; Gao et al., 2016). The *in situ* Hf and O isotope analyses of zircon cores and rims in our granite give quite distinct compositions, suggesting different origins.

The residual zircon cores show highly variable U–Pb ages from 133 to 363 Ma, negative $\varepsilon_{Hf}(t)$ values of –11.7 to –3.5, two-stage Hf model (T_{DM2}) ages of 1595 to 1932 Ma, and higher $\delta^{18}O$ values of 8.62 to 9.78‰. These features indicate that the granite was derived from partial melting of sedimentary rocks, whose crustal provenance was produced by felsic magmatism in the Late Devonian to Early Cretaceous and the original crust was generated via the crust-mantle differentiation in the Middle to Late Paleoproterozoic.

On the other hand, the zircon rims in the granite have concordant ages of 76.1 to 80.5 Ma with an average of 79.1±0.5 Ma, positive $\varepsilon_{Hf}(t)$ values of 5.6 to 11.9, single-stage Hf model ages of 221 to 538 Ma with a peak at ~350 Ma, and lower $\delta^{18}O$ values of 6.06 to 7.05‰. These features demonstrate that the granite was derived from reworking of the juvenile crust in the Late Cretaceous. Zircons from our pegmatite have concordant U-Pb ages of 76.0 to 78.3 Ma with an average of ~76.8±0.4 Ma, positive $\varepsilon_{Hf}(t)$ values of 9.0 to 10.4. The corresponding single-stage Hf model ages are 341 to 365 Ma with a peak at ~356 Ma, and $\delta^{18}O$ values of 5.19 to 6.00‰. These signatures are very similar to those of the magmatic rims of zircon from the granite, indicating that they share the same source of the juvenile crust during the partial melting. In addition, the $\delta^{18}O$ values of garnet and quartz from the pegmatite are also similar to those from the granite, and yield a similar O isotope temperature of 645 °C in view of the uncertainties of ±30-50°C (Zheng, 1993). Therefore, the pegmatite and granite would have crystallized from the same composition of granitic magmas.

However, the major and trace element profiles in the garnets from the pegmatite indicate two generations of garnet growth. The first generation (Grt-I domains) was precipitated from a magmatic–hydrothermal fluid. The slightly lower zircon $\delta^{18}O$ values for the pegmatite relative to the granite zircon imply that the magmatic–hydrothermal fluid would have more evolved than the magmatic fluid when the granitic magmas were emplaced into the upper crust. The second generation of garnet (Grt-II domains) in the pegmatite grew from the same composition of granitic magmas as the granitic garnets. The early Grt-I domains were partly dissolved at this time, patchily replaced by Grt-II, with Grt-II overgrowths crystallizing as rims in the presence of the granitic magmas. Therefore, the pegmatite may have formed before the solidification of granitic magmas, which is consistent with the field observation that the pegmatite is intruded by the granite (Fig. 2a). However, the almost identical zircon U–Pb ages and Hf–O isotope compositions, as well as the almost identical major and trace element compositions of Grt-II domains in both granite and pegmatite, indicate that the pegmatite and granite were crystallized from the differently evolved granitic magmas. The identical U–Pb ages show that the time interval between these evolved magmas was too short to be distinguished from each other.

It is commonly accepted that pegmatites form at the terminal stage of the fractional crystallization of granitic magmas with fluid saturation (Anderson, 2012). The pegmatite and granite studied in this study share the similar pressure and temperature of magma crystallization. However, the differences in major and trace elements between the pegmatitic and granitic garnets suggest an earlier crystallization of pegmatite and a later mixture with the surrounding granitic magma. Therefore, the relationship between pegmatite and its associated granite in the field may not imply the later stage of pegmatite after granite. The elements and isotopes in whole-rock and minerals (such as garnet and zircon) can be used as good indicators of melt evolution. The characteristics of Grt-I domains in the pegmatite suggest that the pegmatite was precipitated from the magmatic–hydrothermal fluids, which were not evolved from the granitic melts. Nevertheless, the similarities in their zircon Hf–O isotope compositions indicate that both pegmatite and granite were derived from partial melting of the same crustal material in Gangdese orogen. In view of the similarities in zircon U–Pb ages and Hf–O isotope compositions between the pegmatite-granite association (this study) and the Gangdese mafic igneous rocks of Late Cretaceous (Tang et al., 2019), it appears that both pegmatite and granite were produced by partial melting of the juvenile continental arc crust along this newly accreted continental margin.

Both granite and pegmatite were emplaced at 76-81 Ma, indicating that this episode of granitic magmatism in the Gangdese orogen predates the collisional orogeny at 55±10 Ma between the Indian and Asian continents (Zheng and Wu, 2018). Because the Gangdese orogen acted as the hangwall of the subducting Indian continent in the Early Cenozoic, the Late Cretaceous magmatism at 76-81 Ma was caused by subduction of the Neo-Tethyan oceanic slab prior to the closure of Neo-Tethyan Ocean. During this episode of felsic magmatism, the preexisting continental arc juvenile crust was reworked via partial melting to produce the evolved continental crust along the convergent plate boundary. Numerous studies of the Langxian granitoids have demonstrated that there was a "flare-up" of magmatic activity at 85–75 Ma (Wen et al., 2008b; Ji et al., 2014; Zhu et al., 2019), which has been ascribed to flat subduction of the Neo-Tethyan oceanic slab (Wen et al., 2008a, 2008b). However, flat subduction leads to compressional heating, which disfavor crustal anataxis in active continental margins (Zheng and Chen, 2016). Instead, steep subduction for extensional heating can induce crustal anataxis in active continental margins (Zheng, 2019). In this regard, the subducting Neo-Tethyan oceanic slab would have rolled back at that time in order to produce the extensional regime for this episode of crustal anatexis in the Gangdese orogen.

ACKNOWLEDGMENTS

This study was supported by funds from the B-type Strategic Priority Program of the Chinese Academy of Sciences (XDB41000000) and the National Natural Science Foundation of China (41822201 and 41772048). Thanks are due to Yixin Liu for her assistance with EMP analyses, to Wenlong Liu for his assistance with the SEM imaging, to Qi Chen for his assistance with the operation of the MC–LA–ICP–MS. We are grateful to Hao Cheng and an anonymous reviewer for their helpful reviews that improve the manuscript.

REFERENCES CITED

Abbott, Jr., R.N. (1981) The role of manganese in the paragenesis of magmatic garnet: an example from the Old Woman-Piute Range, California: a discussion. The Journal of Geology, 89, 767–769.

Amelin, Y., Lee, D.C., Halliday, A.N., and Pidgeon, R.T. (1999) Nature of the earth's earliest crust from hafnium isotopes in single detrital zircons. Nature, 399, 252–255.

Amelin, Y., Lee, D.C., and Halliday, A.N. (2000) Early-middle Archean crustal evolution deduced from Lu–Hf and U–Pb isotopic studies of single zircon grains. Geochimica et Cosmochimica Acta, 64, 4205–4225.

Andersen, T., Griffin, W.L., and Pearson, N.J. (2002) Crustal evolution in the SW part of the Baltic Shield: the Hf isotope evidence. Journal of Petrology, 43, 1725–1747.

Anderson, J.L. (2012) Cold pegmatite. Elements, 8, 248-248.

Arredondo, E.H., Rossman, G.R., and Lumpkin, G.R. (2001) Hydrogen in spessartine-almandine garnets as a tracer of granitic pegmatite evolution. American Mineralogist, 86, 485–490.

Aydar, E., and Gourgaud, A. (2002) Garnet-bearing basalts: an example from Mt. Hasan, Central Anatolia, Turkey. Mineralogy and Petrology, 75, 185–201.

Baldwin, J.R., and Von Knorring, O. (1983) Compositional range of Mn-garnet in zoned granitic pegmatites. The Canadian Mineralogist, 21, 683–688.

Baxter, E.F., and Scherer, E.E. (2013) Garnet geochronology: Timekeeper of tectonometamorphic processes. Elements, 9, 433–438.

Baxter, E.F., Caddick, M.J., and Dragovic, B. (2017) Garnet: A Rock-Forming Mineral Petrochronometer. Reviews in Mineralogy and Geochemistry, 83, 469–533.

Blichert-Toft, J., Chauvel, C., and Albarède, F. (1997) Separation of Hf and Lu for high-precision isotope analysis of rock samples by magnetic sector-multiple collector ICP–MS. Contributions to Mineralogy and Petrology, 127, 248–260.

Caddick, M.J., and Kohn, M.J. (2013) Garnet: Witness to the evolution of destructive plate boundaries. Elements, 9, 427–432.

Caddick, M.J., Konopásek, J., and Thompson, A.B. (2010) Preservation of garnet growth zoning and the duration of prograde metamorphism. Journal of Petrology, 53, 2327–2347.

Carlson, W., and Schwarze, E. (1997) Petrological significance of prograde homogenization of growth zoning in garnet: an example from the Llano Uplift. Journal of Metamorphic Geology, 15, 631–644.

Carlson, W.D. (2002) Scales of disequilibrium and rates of equilibration during metamorphism. American Mineralogist, 87, 185–204.

Chen, Y.-X., Zhou, K., Zheng, Y.-F., Chen, R.-X., and Hu, Z.C. (2015) Garnet geochemistry records the action of metamorphic fluids in ultrahigh-pressure dioritic gneiss from the Sulu orogen. Chemical Geology, 398, 46–60.

Cheng, H., Nakamura, E., Kobayashi, K., and Zhou, Z. (2007) Origin of atoll garnets in eclogites and implications for the redistribution of trace elements during slab exhumation in a continental subduction zone. American Minerologist, 92, 119–1129.

Cheng, H., Bloch, E.M., Moulas, E., and Vervoort, J.D. (2020). Reconciliation of discrepant U–Pb, Lu–Hf, Sm–Nd, Ar–Ar and U–Th/He dates in an amphibolite from the Cathaysia Block in Southern China. Contributions to Mineralogy and Petrology, 175, 4. https://doi.org/10.1007/s00410-019-1644-9.

Chu, M.F., Chung, S.L., Song, B., Liu, D.Y., O'Reilly, S.Y., Pearson, N.J., Ji, J.Q., and Wen, D.J. (2006) Zircon U–Pb and Hf isotope constraints on the Mesozoic tectonics and crustal evolution of southern Tibet. Geology, 34, 745–748.

Chung, S.L., Liu, D.Y., Ji, J.Q., Chu, M.F., Lee, H.Y., Wen, D.J., Lo, C.H., Lee, T.Y., Qian, Q., and Zhang, Q. (2003). Adakites from continental collision zones: melting of thickened lower crust beneath southern Tibet. Geology, 31, 1021–1024.

Chung, S.L., Chu, M.F., Zhang, Y., Xie, Y., Lo, C.H., Lee, T.Y., Lan, C.Y., Li, X., Zhang, Y.Q., and Wang, Y. (2005). Tibetan tectonic evolution inferred from spatial and temporal variations in post-collisional magmatism. Earth Science Reviews, 68, 173–196.

Chung, S.L., Chu, M.F., Ji, J.Q., O'Reilly, S.Y., Pearson, N.J., Liu, D.Y., Lee, T.L., and Lo, C.H. (2009) The nature and timing of crustal thickening in Southern Tibet: geochemical and zircon Hf isotopic constraints from postcollisional adakites. Tectonophysics, 477, 36–

48.

Dahlquist, J.A., Galindo, C., Pankhurst, R.J., Rapela, C.W., Alasino, P.H., Saavedra, J., and Fanning, C.M. (2007). Magmatic evolution of the Penon Rosado Granite: Petrogenesis of garnet bearing granitoids. Lithos, 95, 177–207.

Debon, F., Le Fort, P., Sheppard, S.M., and Sonet, J. (1986) The four plutonic belts of the Transhimalaya–Himalaya: a chemical, mineralogical, isotopic, and chronological synthesis along a Tibet–Nepal section. Journal of Petrology, 27, 219–250.

Deer, W.A., Howie, R.A., and Zussman, J. (1992) An introduction to the rock-forming minerals, 2nd edition. Longmans, London.

Dewey, J.F., Shackleton, R.M., Chang, C.F., and Sun, Y.Y. (1988) The tectonic evolution of the Tibetan Plateau. Philosophical Transactions of the Royal Society of London (Series A): Mathematical and Physical Sciences, 327, 379–413.

Dong, X., Zhang, Z.M., Liu, F. He, Z.Y., and Lin, Y.H. (2014). Late Paleozoic intrusive rocks from the southeastern Lhasa terrane, Tibetan Plateau, and their Late Mesozoic metamorphism and tectonic implications. Lithos, 198–199, 249–262.

Dorais, M.J., Pett, T.K., and Tubrett, M. (2009). Garnetites of the Cardigan Pluton, New Hampshire: Evidence for peritectic garnet entrainment and implications for source rock compositions. Journal of Petrology, 50, 1993–2016.

du Bray, E.A. (1988). Garnet compositions and their use as indicators of peraluminous granitoid petrogenesis-southeastern Arabian Shield. Contributions to Mineralogy and Petrology, 100, 205–212.

Dziggel, A., Wulff, K., Kolb, J., Meyer, F.M., and Lahaye, Y. (2009) Significance of oscillatory and bell-shaped growth zoning in hydrothermal garnet: Evidence from the Navachab gold deposit, Namibia. Chemical Geology, 262, 262–276.

Erdmann, S., Jamieson, R. A., and MacDonald, M. A. (2009). Evaluating the origin of garnet, cordierite, and biotite in granitic rocks: a case study from the South Mountain Batholith, Nova Scotia. Journal of Petrology, 50, 1477–1503.

Fisher, C. M., Vercoort J.D., and Hanchar, J.M. (2014) Guidelines for reporting zircon Hf isotopic data by LA-MC-ICPMS and potential pitfalls in the interpretation of these data. Chemical Geology, 363, 125–133.

Gadas, P., Novak, M., Talla, D., and Galioca, M.V. (2013) Compositional evolution of grossular garnet from leucotonalitic pegmatite at Ruda nad Moravou, Czech Republic; a complex EMPA, LA–ICP–MS, IR and CL study. Mineralogy and Petrology, 107, 311–326.

Ganguly, J., Cheng, W., and Chakraborty, S. (1998) Cation diffusion in aluminosilicate garnets: experimental determination in pyrope–almandine diffusion couples. Contributions to Mineralogy and Petrology, 131, 171–180.

Gao, S., Liu, X.M., Yuan, H.L., Hattendorf, B., Günther, D., Chen, L., and Hu, S.H. (2002) Determination of forty-two major and trace elements in USGS and NIST SRM glasses by laser ablation-inductively coupled plasma-mass spectrometry. Geostandards Newsletter, 26, 181–195.

Gao, P., Zheng, Y.-F., and Zhao, Z.-F. (2016) Distinction between S-type and peraluminous I-type granites: Zircon versus whole-rock geochemistry. Lithos, 258–259, 77–91.

García-Casco, A., Torres-Roldán, R.L., Millán, G., Monié, P., and Schneider, J. (2002) Oscillatory zoning in eclogitic garnet and amphibole, Northern Serpentinite Melange, Cuba: a record of tectonic instability during subduction? Journal of Metamorphic Geology, 20, 581–598.

Gaspar, M., Knaack, C., Meinert, L.D., and Moretti, R. (2008) REE in skarn systems: a LA-ICPMS study of garnets from the Crown Jewel Deposit. Geochimica et Cosmochimica Acta, 72, 185–205.

Geisler, T., Pidgeon, R. T., Kurtz, R., van Bronswijk, W., and Schleicher, H. (2003) Experimental hydrothermal alteration of partially metamict zircon. American Mineralogist, 88, 1496–1513.

Griffin, W.L., Pearson, N.J., Belousova, E., Jackson, S.E., van Achterbergh, E., O'Reilly, S.Y., and Shee, S.R. (2000) The Hf isotope composition of cratonic mantle: LA–MC–ICPMS analysis of zircon megacrysts in kimberlites. Geochimica et Cosmochimica Acta, 64, 133–147.

Griffin, W.L., Wang, X., Jackson, S.E., Pearson, N.J., O'Reilly, S.Y., Xu, X., and Zhou, X. (2002) Zircon chemistry and magma mixing, SE China: in-situ analysis of Hf isotopes. Tonglu and Pingtan igneous complexes. Lithos, 61, 237–269.

Harris, N.B.W., Xu, R.H., Lewis, C.L., and Jin, C.W. (1988a) Plutonic rocks of the 1985 Tibet Geotraverse, Lhasa to Golmud. Philosophical transactions of the Royal Society of London. Series A, mathematical and physical. Sciences, 327, 145–168.

Harris, N.B.W., Holland, T.J.B., and Tindle, A.G. (1988b) Metamorphic rocks of the 1985 Tibet Geotraverse, Lhasa to Golmud. Philosophical Transactions of the Royal Society of London Series A-Mathematical Physical and Engineering Sciences, 327, 203–213.

Harris, N.B.W., Inger, S., and Xu, R.H. (1990) Cretaceous plutonism in Central Tibet: an example of post-collision magmatism? Journal of Volcanology and Geothermal

Research, 44, 21–32.

Hickmott, D., and Spear, F.S. (1992) Major- and trace-element zoning in garnets from calcerous pelites in the NW Shelburne Falls Quadrangle, Massachusetts: garnet growth histories in retrograded rocks. Journal of Petrology, 33, 965–1005.

Hollister, L. S. (1966) Garnet zoning: an interpretation based on the Rayleigh fractionation model. Science, 154, 1647–1651.

Hu, Z.C, Liu, Y. S., Gao S., Hu S.H., Dietiker R., and Günther D. (2008a) A Local Aerosol Extraction Strategy for the Determination of the Aerosol Composition in Laser Ablation Inductively Coupled Plasma Mass Spectrometry. Journal of Analytical Atomic Spectrometry, 23, 1192–1203.

Hu, Z.C., Gao S., Liu, Y. S., Hu, S.H., Chen, H.H., and Yuan, H.L. (2008b) Signal Enhancement in Laser Ablation ICP-MS by Addition of Nitrogen in the Central Channel Gas. Journal of Analytical Atomic Spectrometry, 23, 1093–1101.

Hu, Z.C, Liu, Y. S., Gao S., Xiao, S.Q., Zhao, L.S., Günther, D., Li, M., Zhang, W., and Zong, K.Q. (2012a) A "wire" signal smoothing device for laser ablation inductively coupled plasma mass spectrometry analysis. Spectrochimica Acta Part B, 78, 50–57.

Hu, Z.C, Liu, Y. S., Gao S., Liu, W.G., Yang, L., Zhang, W., Tong, X.R., Lin, L., Zong, K.Q., Li, M., Chen, H.H., Zhou, L., and Yang, L. (2012b) Improved in situ Hf isotope ratio analysis of zircon using newly designed X skimmer cone and Jet sample cone in combination with the addition of nitrogen by laser ablation multiple collector ICP-MS. Journal of Analytical Atomic Spectrometry, 27, 1391–1399.

Jamtveit, B., and Anderson, T.B. (1992) Morphological instabilities during rapid growth of metamorphic garnets. Physics and Chemistry of Minerals, 19, 176–184.

Ji, W.Q., Wu, F.Y., Chung, S.L., Li, J.X., and Liu, C.Z. (2009). Zircon U–Pb geochronological and Hf isotopic constraints on petrogenesis of the Gangdese batholith in Tibet. Chemical Geology, 262, 229–245.

Ji, W.Q., Wu, F.Y., Chung, S.L., and Liu, C.Z. (2014). The Gangdese magmatic constraints on a latest Cretaceous lithospheric delamination of the Lhasa terrane, southern Tibet. Lithos, 210–211, 168–180.

Kawabata, H., and Takafuji, N. (2005) Origin of garnet crystals in calc–alkaline volcanic rocks from the Setouchi volcanic belt, Japan. Mineralogical Magazine, 69, 951–971.

Kohn, M.J., Spear, F.S., and Valley, J.W. (1997). Dehydration-melting and fluid recycling during metamorphism. Rangely Formation, New Hampshire, USA. Journal of Petrology, 38, 1255–1277.

Kohn, M.J. (2003) Geochemical zoning in metamorphic minerals. In: Rudnick RL (ed.) Treatise on Geochemistry, vol. 3, pp. 229–261. Oxford: Elsevier.

Kohn, M.J. (2004) Oscillatory- and sector-zoned garnets record cyclic (?) rapid thrusting in central Nepal. Geochemistry, Geophysics, Geosystems 5: Q12014. http://dx.doi.org/10.1029/2004GC000737.

Konrad-Schmolke, M., Zack, T., O'Brien, P.J., and Jacob, D.E. (2008a). Combined thermodynamic and rare earth element modeling of garnet growth during subduction: Examples from ultrahigh–pressure eclogite of the Western Gneiss Region, Norway. Earth and Planetary Science Letters, 272, 488–498.

Konrad-Schmolke, M., O'Brien, P.J., de Capitani, C., and Carswell, D.A. (2008b). Garnet growth at high– and ultra–high pressure conditions and the effect of element fractionation on mineral modes and composition. Lithos, 103, 309–332.

Lackey, J.S., Romero, G.A., Bouvier, A.S., and Valley, J.W. (2012). Dynamic growth of garnet in granitic magmas. Geology, 40, 171–174.

Li, Z.X., Li, X.H., Wartho, J.A., Clark, C., Li, W.X., Zhang, C.L., and Bao, C. (2010a). Magmatic and metamorphic events during the early Paleozoic Wuyi-Yunkai orogeny, southeastern South China: new age constraints and pressure–temperature conditions. Geological Society of America Bulletin, 122, 772–793.

Li, Q.L., Li, X.H., Liu, Y., Tang, G.Q., Yang, J.H., and Zhu, W.G. (2010b). Precise U–Pb and Pb–Pb dating of Phanerozoic baddeleyite by SIMS with oxygen flooding technique. Journal of Analytical Atomic Spectrometry, 25, 1107–1113.

Li, X.H., Tang, G.Q., Gong, B., Yang, Y.H., Hou, K.J., Hu, Z.C., Li, Q.L., Liu, Y., and Li, W.X. (2013) Qinghu zircon: a working reference for microbeam analysis of U–Pb age and Hf and O isotopes. Chinese Science Bulletin, 58, 4647–4654.

Liu, Y.S., Hu, Z.C., Gao, S., Günther, D., Xu, J., Gao, C.G., and Chen, H.H. (2008). In situ analysis of major and trace elements of anhydrous minerals by LA–ICP–MS without applying an internal standard. Chemical Geology, 257, 34–43.

Liu, Y. S., Gao, S., Hu, Z., Gao, C., Zong, K., and Wang, D. (2010a). Continental and oceanic crust recycling-induced melt peridotite interactions in the Trans–North China Orogen: U–Pb dating, Hf isotopes and trace elements in zircons of mantle xenoliths. Journal of Petrology, 51, 537–571.

Liu, Y.S., Hu, Z.C., Zong, K.Q., Gao, C.G., Gao, S., Xu, J., and Chen, H.H. (2010b). Reappraisement and refinement of zircon U–Pb isotope and trace element analyses by LA–ICP–MS. Chinese Science Bulletin, 55, 1535–1546.

London, D. (2008) Pegmatites. Canadian Mineralogist, Special Publication, 10. p 347.

London, D., and Kontak, D.J. (2012) Granitic pegmatites: Scientific wonders and economic bonanzas. Elements, 8, 257–261.

Ludwig, K.R. (2003) User's Manual for Isoplot 3.00: A Geochronological Toolkit for Microsoft Excel. Berkeley Geochronology Center Special Publication, Berkeley. No. 4, 70 pp.

Ma, L., Wang, Q., Li, Z.X., Wyman, D.A., Jiang, Z.Q., Yang, J.H., Gou, G.N., and Guo, H.F. (2013a) Early Late Cretaceous (ca. 93Ma) norites and hornblendites in the Milin area, eastern Gangdese: Lithosphere-asthenosphere interaction during slab roll-back and an insight into early Late Cretaceous (ca. 100–80Ma) magmatic “flare-up” in southern Lhasa (Tibet). Lithos, 172–173, 17–30.

Ma, L., Wang, Q., Li, Z.X., Wyman, D.A., Jiang, Z.Q., Yang, J.H., Gou, G.N., and Guo, H.F. (2013b) Late Cretaceous (100–89 Ma) magnesian charnockites with adakitic affinities in the Milin area, eastern Gangdese: partial melting of subducted oceanic crust and implications for crustal growth in southern Tibet. Lithos, 175–176, 315–332.

Ma, L., Wang, Q., Wyman, D.A., Jiang, Z.Q., Yang, J.H., Li, Q.-L., Gou, G.N., and Guo, H.F. (2013c) Late Cretaceous crustal growth in the Gangdese area, southern Tibet: Petrological and Sr–Nd–Hf–O isotopic evidence from Zhengga diorite-gabbro. Chemical Geology, 349–350, 54–70.

Manning, D.A. (1983) Chemical variation in garnets from aplites and pegmatites, peninsular Thailand. Mineralogical Magazine, 47, 353–358.

McDonough, W.F., and Sun, S. (1995) The composition of the Earth. Chemical Geology, 120, 223–253.

Melo, M.G., Lana, C., Steven, G., Pedrosa-Soares, A.C., Gerdes, A., Alkmin, L.A., Nalini Jr., H.A., and Alkmim, F.F. (2017). Assessing the isotopic evolution of S-type granites of the Carlos Chagas Batholith, SE Brazil: Clues from U–Pb, Hf isotopes, Ti geothermometry and trace element composition of zircon. Lithos, 284–285, 730–750.

Miller, C. F., and Stoddard, E. F. (1981). The role of manganese in the paragenesis of magmatic garnet: an example from the Old Woman-Piute Range, California. Journal of Geology, 89, 233–246.

Mirnejad, H., Blourian, G.H., Kheirkhah, M., Akrami, M.A., and Tutti, F. (2008) Garnet-bearing rhyolite from Deh-Salm area, Lut block, Eastern Iran: anatexis of deep crustal rocks. Mineralogy and Petrology, 94, 259–269.

Mo, X.X., Hou, Z.Q., Niu, Y.L., Dong, G.C., Qu, X.M., Zhao, Z.D., and Yang, Z.M. (2007)

Mantle contributions to crustal thickening during continental collision: evidence from Cenozoic igneous rocks in Southern Tibet. Lithos, 96, 225–242.

Moretz, L., Heimann, A., Bitner, J., Wise, M., Rodrigues Soares, D., and Mousinho Ferreira, A. (2013) The composition of garnet as indicator of rare metal (Li) mineralization in granitic pegmatites. Proceeding of The 6th International Symposium on Granitic Pegmatites, pp. 94–95.

Muller, A., Kearsley, A., Spratt, J., and Seltmann, R. (2012) Petrogenetic implications of magmatic garnet in granitic pegmatites from southern Norway. The Canadian Mineralogist, 50, 1095–1115.

Narduzzi, F., Farina, F., Stevens, G., Lana, C., and Nalini Jr., H.A. (2017) Magmatic garnet in the Cordilleran-type Galiléia granitoids of the Araçuaí belt (Brazil): Evidence for crystallization in the lower crust. Lithos, 282–283, 82–97.

Otamendi, J.E., de la Rosa, J.D., Patiño Douce, A.E. and Castro, A. (2002). Rayleigh fractionation of heavy rare earths and yttrium during metamorphic garnet growth. Geology, 30, 159–162.

Pan, G.T., Mo, X.X., Hou, Z.Q., Zhu, D.C., Wang, L.Q., Li, G.M., Zhao, Z.D., Geng, Q.R., and Liao, Z. L. (2006). Spatial-temporal framework of the Gangdese Orogenic Belt and its evolution. Acta Petrologica Sinica, 22, 521–533 (In Chinese with English abstract).

Pan, G.T., Wang, L.Q., Li, R.S., Yuan, S.H., Ji, W.H., Yin, F.G., Zhang, W.P., and Wang, B.D. (2012) Tectonic evolution of the Qinghai-Tibet Plateau: Journal of Asian Earth Sciences, 53, 3–14.

Pearce, J.A., and Deng, W.M. (1988) The ophiolites of the Tibetan Geotraverse, Lhasa to Golmud (1985) and Lhasa to Kathmandu (1986). Philosophical Transactions of the Royal Society of London, Series A, Mathematical and Physical Sciences, 327, 215–238.

Ravikant, V., Wu, F.Y., and Ji, W.Q. (2009) Zircon U–Pb and Hf isotopic constraints on petrogenesis of the Cretaceous–Tertiary granites in eastern Karakoram and Ladakh, India. Lithos, 110, 153–166.

Rubatto, D., Müntener, O., Barnhorn, A., and Gregory, C. (2008). Dissolution-reprecipitation of zircon at low-temperature, high-pressure conditions (Lanzo Massif, Italy). American Mineralogist, 93, 1519–1529.

Samadi, R., Miller, N.R., Mirnejad, H., Harris, C., Kawabata, H., and Shirdashtzadeh, N. (2014a). Origin of garnet in aplite and pegmatite from Khajeh Morad in northeastern Iran: A major, trace element, and oxygen isotope approach. Lithos, 208–209, 378–392.

Samadi, R., Mirnejad, H., Kawabata, H., Valizadeh, M.V., Harris, C., and Gazel, E. (2014b)

Magmatic garnet in the Triassic (215 Ma) Dehnow pluton of NE Iran and its petrogenetic significance. International Geology Review, 56, 596–621.

Samson, S.D., D'Lemos, R.S., Blichert-Toft, J., and Vervoort, J. (2003) U–Pb geochronology and Hf–Nd isotope compositions of the oldest Neoproterozoic crust within the Cadomian orogen: new evidence for a unique juvenile terrane. Earth and Planetary Science Letters, 208, 165–180.

Searle, M.P., Windley, B.F., Coward, M.P., Cooper, D.J.W., Rex, A.J., Rex, D., Li, T.D., Xiao, X.C., Jan, M.Q., Thakur, V.C., and Kumar, S. (1987) The closing of Tethys and the tectonics of the Himalaya. Geological Society of America Bulletin, 98, 678–701.

Segal, I., Halicz, L., and Platzner, I.T. (2003) Accurate isotope ratio measurements of ytterbium by multiple collection inductively coupled plasma mass spectrometry applying erbium and hafnium in an improved double external normalization procedure. Journal of Analytical Atomic Spectrometry, 18, 1217–1223.

Simmons, W.B., and Webber, K.L. (2008) Pegmatite genesis: state of the art. European Journal of Mineralogy, 20, 421–438.

Smith, M.P., Henderson, P., Jeffries, T.E.R., Long, J., and Williams, C.T. (2004) The rare earth elements and uranium in garnet from the Beinn an Dubhaich aureole, Skye, Scottland, UK: constraints on processes in a dynamic hydrothermal system. Journal of Petrology, 45, 457–484.

Spear, F.S., and Kohn, M.J. (1996) Trace element zoning in garnet as a monitor of crustal melting. Geology, 24, 1099–1102.

Stevens, G., Villaros, A., and Moyen, J.F. (2007) Selective peritectic garnet entrainment as the origin of geochemical diversity in S-type granites. Geology, 35, 9–12.

Sun, S.-s., and McDonough, W.F. (1989) Chemical and isotopic systematics of oceanic basalt: implications for mantle composition and processes. Geological Society Special Publication, 42, 313–345.

Tang, Y.-W., Cheng, L., Zhao, Z.-F., and Zheng, Y.-F. (2019) Geochemical evidence for the production of granitoids through reworking of the juvenile mafic arc crust in the Gangdese orogen, southern Tibet. Geological Society of America Bulletin. https://doi.org/10.1130/B35304.1.

Thomas, R., and Davidson, P. (2012) Water in granite and pegmatite-forming melts. Ore Geology Reviews, 46, 32–46.

Thöni, M., and Miller, C. (2004) Ordovician meta-pegmatite garnet (NW Ötztal basement, Tyrol, Eastern Alps): preservation of magmatic garnet chemistry and Sm-Nd age during mylonitization. Chemical Geology, 209, 1–26.

Thöni, M., Petrík, I., Janák, M., and Lupták, B. (2003) Preservation of Variscan garnet in Alpine metamorphosed pegmatite from the Veporic Unit, Western Carpathians: evidence from Sm-Nd isotope data. Journal of the Czech Geological Society, 48, 123–124.

Valley, J.W. (2003) Oxygen isotopes in zircon. Reviews in Mineralogy and Geochemistry, 53, 343–385.

Valley, J.W., Kinny, P.D., Schulze, D.J., and Spicuzza, M.J. (1998) Zircon megacrysts from kimberlite: oxygen isotope variability among mantle melts. Contributions to Mineralogy and Petrology, 133, 1–11.

Villaros, A., Stevens, G., and Buick, I.S. (2009) Tracking S-type granite from source to emplacement: Clues from garnet in the Cape Granite Suite. Lithos, 112, 217–235.

Wang, J.L., Zhang, Z.M., and Shi, C. (2008). Anatexis and dynamics of the southeastern Lhasa terrane. Acta Petrologica Sinica, 24, 1539–1551.

Wang, L., Zeng, L.S., Gao, L.E., and Chen, Z.Y. (2013) Early Cretaceous high Mg# and high Sr/Y clinopyroxene-bearing diorite in the southeast Gangdese batholith, Southern Tibet Yanshi Xuebao, 29, 1977–1994. (In Chinese with English abstract)

Watson, E.B., Wark, D.A., and Thomas, J.B. (2006) Crystallization thermometers for zircon and rutile. Contributions to Mineralogy and Petrology, 151, 413–433.

Wen, D.-R. (2007) The Gangdese Batholith, Southern Tibet: Ages, Geochemical Characteristics and Petrogenesis. (PhD thesis) National Taiwan University (140 pp.).

Wen, D.-R., Liu, D., Chung, S.-L., Chu, M.-F., Ji, J., Zhang, Q., Song, B., Lee, T.-Y., Yeh, M.-W., and Lo, C.-H. (2008a). Zircon SHRIMP U–Pb ages of the Gangdese batholith and implications for Neotethyan subduction in southern Tibet. Chemical Geology, 252, 191–201.

Wen, D.R., Chung, S.L., Song, B., Iizuka, Y., Yang, H.J., Ji, J.Q., Liu, D.Y., and Gallet, S. (2008b) Late Cretaceous Gangdese intrusions of adakitic geochemical characteristics, SE Tibet: petrogenesis and tectonic implications. Lithos, 105, 1–11.

Whitney, D.L., and Evans, B.W. (2010) Abbreviations for names of rock-forming minerals. American Mineralogist, 95, 185–187.

Whitworth, M.P. (1992) Petrogenetic implications of garnets associated with lithium pegmatites from SE Ireland. Mineralogical Magazine, 56, 75–83.

Wiedenbeck, M., Alle, P., Corfu, F., Griffin, W.L., Meier, M., Oberli, F., Quadt, A.V., Roddick, J.C., and Spiegel, W. (1995) Three natural zircon standards for U–Th–Pb, Lu–Hf, trace element and REE analyses. Geostandards and Geoanalytical Research, 19, 1–

23.

Woodhead, J., Hergt, J., Shelley, M., Eggins, S., and Kemp, R. (2004) Zircon Hf–isotope analysis with an excimer laser, depth profiling, ablation of complex geometries, and concomitant age estimation Chemical Geology, 209, 121–135.

Xia, Q.-X., Wang, H.-Z., Zhou, L.-G., Gao, X.-Y., Van Orman, J.A., Zheng, Y.-F., Xu, H.J., and Hu, Z.C. (2016). Growth of metamorphic and peritectic garnets in ultrahigh–pressure metagranite during continental subduction and exhumation in the Dabie orogen. Lithos, 266–267, 158–181.

Xia, Q.-X., Gao, P., Yang, G., Zheng, Y.-F., Zhao, Z.-F., Li, W.-C., and Luo, X. (2020) The origin of garnets in anatectic rocks from the eastern Himalayan syntaxis, southeastern Tibet： Constraints from major and trace element zoning and phase equilibrium relationships. Journal of Petrology, 61, doi: 10.1093/petrology/egaa009.

Xu, R.H., Schärer, U., and Allègre, C.J. (1985) Magmatismand metamorphism in the Lhasa block (Tibet): a geochronological study. Journal of Geology, 93, 41–57.

Yin, A., and Harrison, T.M. (2000). Geologic evolution of the Himalayan Tibetan Orogen. Annual Review of Earth and Planetary Sciences, 28, 211–280.

Zhang, J.Y., Ma, C.Q., and She, Z.B. (2012) An Early Cretaceous garnet-bearing metaluminous A-type granite intrusion in the East Qinling Orogen, central China: Petrological, mineralogical and geochemical constraints. Geoscience Frontiers, 3, 635–646.

Zheng, Y.-F. (1993) Calculation of oxygen isotope fractionation in anhydrous silicate minerals. Geochimica et Cosmochimica Acta, 57, 1079–1091.

Zheng, Y.-F., Fu, B., Li, Y.-L., Xiao, Y.-L., and Li, S.-G. (1998) Oxygen and hydrogen isotope geochemistry of ultrahigh pressure eclogites from the Dabie Mountains and the Sulu terrane. Earth and Planetary Science Letters, 155, 113–129.

Zheng, Y.-F., Wang, Z.-R., Li, S.-G., and Zhao, Z.-F. (2002) Oxygen isotope equilibrium between eclogite minerals and its constraints on mineral Sm–Nd chronometer. Geochimica et Cosmochimica Acta, 66, 625–634.

Zheng, Y.-F., Wu, Y.-B., Chen, F.K., Gong, B., Li, L., and Zhao, Z.-F. (2004) Zircon U–Pb and oxygen isotope evidence for a large–scale ^{18}O depletion event in igneous rocks during the Neoproterozoic. Geochimica et Cosmochimica Acta, 68, 4145–4165.

Zheng, Y.-F., Zhao, Z.-F., Wu, Y.-B., Zhang, S.-B., Liu, X.M., and Wu, F.-Y. (2006) Zircon U–Pb age, Hf and O isotope constraints on protolith origin of ultrahigh–pressure eclogite and gneiss in the Dabie orogen. Chemical Geology, 231, 135–158.

Zheng, Y.-F., Chen, R.-X., and Zhao, Z.-F. (2009) Chemical geodynamics of continental subduction-zone metamorphism: Insights from studies of the Chinese Continental Scientific Drilling (CCSD) core samples. Tectonophysics, 475, 327–358.

Zheng, Y.-F., Xiao, W.J., and Zhao, G.C. (2013) Introduction to tectonics of China. Gondwana Research, 23, 1189–1206.

Zheng, Y.-F., and Chen, Y.-X. (2016) Continental versus oceanic subduction zones. National Science Review, 3, 495–519.

Zheng, Y.-F., and Wu, F.-Y. (2018) The timing of continental collision between India and Asia. Science Bulletin, 63, 1649–1654.

Zheng, Y.-F. (2019) Subduction zone geochemistry. Geoscience Frontiers, 10, 1223-1254.

Zheng, Y.-F., Mao, J.W., Chen, Y.J., Sun, W.D., Ni, P., and Yang, X.Y. (2019) Hydrothermal ore deposits in collision orogens. Science Bulletin, 64, 205–212.

Zhou, L.-G., Xia, Q.-X., Zheng, Y.-F., and Chen, R.-X. (2011). Multistage growth of garnet in ultrahigh–pressure eclogite during continental collision in the Dabie orogen: constrained by trace elements and U–Pb ages. Lithos, 127, 101–127.

Zhu, D.C., Zhao, Z.D., Niu, Y.L., Mo, X.X., Chung, S.L., Hou, Z.Q., Wang, L.Q., and Wu, F.Y. (2011). The Lhasa Terrane: Record of a microcontinent and its histories of drift and growth. Earth and Planetary Science Letters, 301, 241–255.

Zhu, D.C., Zhao, Z.D., Niu, Y., Dilek, Y., Hou, Z.Q., and Mo, X.X. (2012) The origin and pre–Cenozoic evolution of the Tibetan Plateau. Gondwana Research, 23, 1429–1454.

Zhu, D.C., Wang, Q., Chung, S.-L., Cawood, P.A., and Zhao, Z.-D. (2019) Gangdese magmatism in southern Tibet and India–Asia convergence since 120 Ma, in Treloar, P.J., and Searle, M.P., eds., Himalayan Tectonics: A Modern Synthesis: Geological Society of London, Special Publication, 483, 583–604.

Zong, K., Liu, Y., Hu, Z., Kusky, T., Wang, D., Gao, C., Gao, S., and Wang, J. (2010) Melting–induced fluid flow during exhumation of gneisses of the Sulu ultrahigh–pressure terrane. Lithos, 120, 490–510.

Supplementary Table

Table S1. Whole-rock major and trace element compositions of the granite and pegmatite from the Gangdese orogen.

Figure Captions

Fig. 1. (a) Sketch map of the geology of the Himalayan–Tibetan Plateau; (b) Distribution of the eastern Gangdese batholith in the Lhasa terrane showing the sampling location (modified after Ji et al., 2014)

Fig. 2. Field photographs of the granite and pegmatite at Langxian in the southeastern Lhasa terrane. (a) Relationship between granite and pegmatite in the outcrop. (b)–(c) Close-up views of the coarse-grained garnet-bearing pegmatite and the fine-grained granite. (d) Samples collected from the pegmatite.

Fig. 3. Photomicrographs of granite (a–b) and pegmatite (c–f). Mineral abbreviations are from Whitney and Evans (2010).

Fig. 4. (a–e) BSE images of garnets from granite and pegmatite. (f–j) Major element profiles of the garnets from EMP analyses. (k–o) Chondrite-normalized REE distributions from LA–ICP–MS analyses. Chondrite values are from Sun and McDonough (1989).

Fig. 5. Mn, Fe, Ca, and Mg mapping of three grains of garnet (G1–G3) from the pegmatite.

Fig. 6. Trace element profiles from LA–ICP–MS analyses of four garnet grains from (a-b) the granite and (c–e) the pegmatite.

Fig. 7. (a–d) CL images, U–Pb concordia diagrams, weighted mean ages, and chondrite-normalized REE distributions for garnets from the granite. (e–h) CL images, U–Pb concordia diagrams, weighted mean ages, and chondrite-normalized REE distributions for garnets from the pegmatite. The numbers in circles denote the analysis numbers, with adjacent values being the corresponding apparent $^{206}Pb/^{238}U$ ages. The oval shapes denote the analyzed O isotopes.

Fig. 8. (a) Plots of zircon $^{176}Lu/^{177}Hf$ ratios versus $^{176}Hf/^{177}Hf$ ratios. (b) Plots of $\varepsilon_{Hf}(t)$ values versus $\delta^{18}O$ values. (c–d) Histograms of Hf model ages for the granite and pegmatite, respectively.

Fig. 9. Comparisons of CaO versus MnO contents (wt.%) for garnets from the granite and pegmatite, and also magmatic garnets from highly evolved granitoids and pegmatites, low-evolved experimental melts, and peritectic garnets from high-pressure (HP) to ultrahigh-pressure (UHP) metamorphic rocks. Data for the garnets from highly evolved granitoids and pegmatites are from Baldwin and Von Knorring (1983), du Bray (1988), Whitworth (1992), Arredondo et al. (2001), Dahlquist et al. (2007), Muller et al. (2012), Zhang et al. (2012), and Samadi et al. (2014a). Data for the garnets from low-evolved melts are from Wang et al. (2008), Xia et al. (2020), and some unpublished data obtained from melting experiments. Data for the HP garnets from M/I-type magmas are from Samadi et al. (2014b). Data for other magmatic garnets are from Thoni and Miller (2004).

Fig. 10. Plots of Y and Yb concentrations versus CaO contents for garnets from the pegmatite. Grt-I and Grt-II refer to the two stages of garnet growth.

Table 1 Representative microprobe data (in wt.%) of garnets and their calculated structural formula based on 12 oxygen atoms from the Gandese orogen.

Sample	12LS257															
Grain	G1						G2				G9					
Spot	1-1	1-3	1-5	1-7	1-9	1-10	2-1	2-3	2-5	2-7	9-1	9-3	9-5	9-7	9-8	9-9
Domain																
SiO_2	36.73	36.22	36.03	36.55	36.36	36.64	36.49	36.57	36.48	35.81	36.85	35.98	36.39	37.23	36.61	36.33
TiO_2	b.d	0.067	0.207	0.235	0.05	0.070	0.075	0.054	0.225	0.024	0.092	0.045	0.053	0.054	0.104	0.072
Al_2O_3	20.34	20.09	19.51	19.75	20.15	19.71	19.96	19.24	19.76	20.11	20.22	19.97	20.18	20.11	20.32	20.05
FeO	18.47	19.58	19.66	19.62	19.34	19.02	19.06	19.03	19.22	18.66	19.80	19.25	19.70	19.77	19.68	19.57
MnO	21.14	20.29	20.66	20.62	20.19	20.29	20.31	20.56	20.68	20.50	20.29	20.36	20.45	19.95	20.53	20.13
MgO	1.064	1.264	1.255	1.228	1.186	1.158	1.253	1.234	1.238	1.198	1.273	1.129	1.116	1.245	1.276	1.271
CaO	1.860	1.982	1.821	1.717	1.779	1.664	1.671	1.593	1.783	1.87	1.712	1.924	2.000	1.983	1.943	1.647
Cr_2O_3	b.d	b.d	0.001	0.025	0.003	b.d	b.d	0.069	0.019	b.d	b.d	0.021	b.d	0.037	b.d	0.003
Total	99.60	99.50	99.15	99.74	99.05	98.55	98.81	98.35	99.41	98.17	100.25	98.68	99.90	100.38	100.44	99.07
Si	3.009	2.977	2.978	2.997	2.997	3.031	3.012	3.036	2.999	2.980	3.001	2.983	2.981	3.023	2.979	2.995
Al^{iv}	-	0.023	0.022	0.003	0.003	-	-	-	0.001	0.020	-	0.017	0.019	-	0.021	0.005
Al^{vi}	1.966	1.928	1.886	1.911	1.958	1.924	1.945	1.887	1.918	1.955	1.945	1.938	1.934	1.927	1.933	1.947
Ti	-	0.004	0.013	0.014	0.003	0.004	0.005	0.003	0.014	0.002	0.006	0.003	0.003	0.003	0.006	0.004
Cr	-	-	-	0.002	-	-	-	0.005	0.001	-	-	0.001	-	0.002	-	-
Fe^{3+}	0.023	0.060	0.089	0.065	0.035	0.035	0.035	0.061	0.059	0.038	0.043	0.051	0.055	0.039	0.054	0.043
Fe^{2+}	1.243	1.286	1.270	1.281	1.299	1.281	1.281	1.260	1.263	1.261	1.306	1.283	1.295	1.303	1.285	1.306
Mn	1.467	1.413	1.447	1.432	1.409	1.422	1.420	1.445	1.440	1.445	1.400	1.430	1.419	1.372	1.415	1.406
Mg	0.130	0.155	0.155	0.150	0.146	0.143	0.154	0.153	0.152	0.149	0.155	0.140	0.136	0.151	0.155	0.156
Ca	0.163	0.175	0.161	0.151	0.157	0.148	0.148	0.142	0.157	0.167	0.149	0.171	0.176	0.173	0.169	0.145
Total	8.000	8.021	8.021	8.006	8.006	7.989	7.998	7.992	8.004	8.016	8.004	8.017	8.018	7.994	8.017	8.008
Sps	49.22	47.46	48.58	48.34	47.14	48.44	47.89	49.46	48.62	48.49	47.04	47.93	47.59	46.55	47.50	47.07
Alm	40.94	41.48	40.81	41.50	42.73	41.67	41.93	40.46	40.95	40.93	42.75	41.66	41.95	42.49	41.62	42.84
Prp	4.36	5.20	5.19	5.07	4.88	4.87	5.20	5.23	5.12	4.99	5.193	4.678	4.571	5.111	5.196	5.229
Grs	4.34	2.85	0.92	1.74	3.51	3.23	3.24	1.47	2.26	3.67	2.867	3.076	3.107	3.748	2.957	2.701
Adr	1.13	3.02	4.50	3.27	1.74	1.80	1.75	3.15	2.98	1.92	2.153	2.585	2.781	1.982	2.731	2.159

Table 1 (Continued)

Sample	12LS258															
Grain	G1								G2							
Spot	A1	A2	A5	A9	A14	A17	A18	A20	B1	B2	B5	B9	B12	B15	B19	B20
Domain																
SiO_2	35.92	36.45	35.88	36.35	35.80	36.16	36.55	36.42	36.72	36.34	36.34	36.22	36.24	36.50	36.56	35.92
TiO_2	0.049	0.06	0.052	0.196	0.188	0.169	0.009	0.057	0.094	0.094	0.18	0.117	0.095	0.063	0.058	0.069
Al_2O_3	20.13	20.26	19.99	19.73	19.94	19.78	20.06	20.10	19.30	19.78	19.54	19.63	19.87	20.10	19.85	20.15
FeO	19.49	20.04	17.14	17.87	18.39	19.46	20.34	19.23	19.35	18.63	17.89	16.62	16.83	17.42	19.89	19.64
MnO	20.80	20.76	23.95	23.16	22.38	21.73	21.29	21.23	21.13	22.20	23.67	24.81	25.10	23.89	20.61	20.927
MgO	1.035	1.038	0.997	1.033	1.034	1.067	1.072	0.873	0.945	1.081	0.99	0.997	0.936	1.037	1.129	1.055
CaO	1.714	1.626	1.228	1.496	1.712	1.277	1.076	1.671	1.700	1.119	1.432	1.406	1.289	1.340	1.570	1.717
Cr_2O_3	b.d	b.d	0.007	b.d	b.d	b.d	b.d	0.027	0.004	b.d	b.d	0.009	0.001	b.d	0.002	0.022
Total	99.14	100.23	99.25	99.84	99.44	99.65	100.39	99.61	99.25	99.24	100.05	99.82	100.36	100.35	99.66	99.49
Si	2.970	2.981	2.969	2.987	2.957	2.980	2.988	2.995	3.029	3.001	2.985	2.981	2.971	2.983	3.002	2.962
Al^{iv}	0.030	0.019	0.031	0.013	0.043	0.020	0.012	0.005	0.000	0.000	0.015	0.019	0.029	0.017	0.000	0.038
Al^{vi}	1.936	1.937	1.924	1.903	1.904	1.907	1.927	1.947	1.882	1.930	1.884	1.893	1.898	1.925	1.926	1.926
Ti	0.003	0.004	0.003	0.012	0.012	0.010	0.001	0.004	0.006	0.006	0.011	0.007	0.006	0.004	0.004	0.004
Cr	-	-	-	-	-	-	-	0.002	-	-	-	0.001	-	-	-	0.001
Fe^{3+}	0.054	0.053	0.064	0.075	0.075	0.073	0.064	0.042	0.073	0.057	0.093	0.088	0.086	0.063	0.060	0.061
Fe^{2+}	1.294	1.318	1.123	1.153	1.195	1.268	1.327	1.281	1.262	1.230	1.136	1.057	1.068	1.128	1.306	1.293
Mn	1.457	1.438	1.679	1.612	1.565	1.517	1.474	1.479	1.476	1.553	1.647	1.730	1.743	1.654	1.433	1.461
Mg	0.128	0.127	0.123	0.127	0.127	0.131	0.131	0.107	0.116	0.133	0.121	0.122	0.114	0.126	0.138	0.130
Ca	0.152	0.142	0.109	0.132	0.151	0.113	0.094	0.147	0.150	0.099	0.126	0.124	0.113	0.117	0.138	0.152
Total	8.024	8.018	8.026	8.014	8.030	8.018	8.018	8.009	7.996	8.007	8.019	8.022	8.027	8.018	8.008	8.028
Sps	49.05	48.23	56.55	54.14	52.94	50.89	49.33	49.48	50.48	52.23	55.58	58.04	58.67	55.44	48.23	49.33
Alm	41.54	42.75	35.65	37.19	37.63	40.92	43.14	42.01	40.41	39.96	36.08	33.70	33.67	36.39	42.47	41.17
Prp	4.30	4.24	4.14	4.25	4.31	4.40	4.37	3.58	3.97	4.48	4.09	4.10	3.85	4.24	4.65	4.38
Grs	2.39	2.14	0.42	0.65	1.33	0.09	-	2.73	1.40	0.48	-	-	-	0.77	1.60	1.97
Adr	2.72	2.64	3.22	3.78	3.80	3.70	3.15	2.11	3.73	2.85	4.25	4.13	3.81	3.16	3.04	3.08

Table 1 (Continued)

Sample				12LS258						
Grain				G3						
Spot	C1	C2	C3	C4	C5	C6	C7	C8	C9	C10
Domain										
SiO_2	36.01	36.20	36.19	36.11	36.72	35.97	36.46	35.62	36.03	36.56
TiO_2	0.08	0	0.055	0.194	0.147	0.058	0.116	0.044	0.006	0.083
Al_2O_3	20.26	19.95	20.07	19.62	19.76	19.86	19.46	19.89	20.21	19.64
FeO	19.74	19.77	17.38	17.30	16.65	16.63	17.11	17.13	18.81	19.70
MnO	20.74	21.33	23.54	23.90	24.30	24.81	24.68	24.41	21.75	20.89
MgO	1.192	1.155	1.043	0.898	0.999	0.837	0.954	0.988	1.211	1.05
CaO	1.572	1.237	1.216	1.687	1.697	1.431	1.364	1.423	1.097	1.666
Cr_2O_3	b.d	b.d	b.d	0.001	b.d	0.021	0.012	0.004	0.026	b.d
Total	99.59	99.64	99.49	99.71	100.26	99.61	100.16	99.52	99.15	99.58
Si	2.963	2.981	2.983	2.976	3.000	2.970	2.992	2.947	2.977	3.007
Al^{iv}	0.037	0.019	0.017	0.024	-	0.030	0.008	0.053	0.023	-
Al^{vi}	1.932	1.922	1.937	1.889	1.909	1.909	1.883	1.895	1.949	1.909
Ti	0.005	0	0.003	0.012	0.009	0.004	0.007	0.003	0	0.005
Cr	-	-	-	-	-	0.001	0.001	-	0.002	-
Fe^{3+}	0.056	0.069	0.053	0.088	0.072	0.076	0.097	0.091	0.043	0.070
Fe^{2+}	1.303	1.292	1.144	1.105	1.066	1.072	1.078	1.095	1.256	1.285
Mn	1.446	1.488	1.643	1.669	1.682	1.735	1.716	1.711	1.522	1.456
Mg	0.146	0.142	0.128	0.110	0.122	0.103	0.117	0.122	0.149	0.129
Ca	0.139	0.109	0.107	0.149	0.149	0.127	0.120	0.126	0.097	0.147
Total	8.026	8.023	8.017	8.022	8.008	8.027	8.018	8.042	8.019	8.007
Sps	48.80	49.92	55.10	56.06	56.75	58.43	58.27	58.03	51.14	49.17
Alm	41.59	41.66	37.01	35.22	34.13	33.83	33.69	33.55	40.59	41.53
Prp	4.93	4.76	4.30	3.71	4.11	3.47	3.96	4.13	5.01	4.35
Grs	1.85	0.18	0.93	0.59	1.37	0.35	-	-	0.99	1.41
Adr	2.82	3.48	2.67	4.41	3.64	3.85	4.03	4.27	2.19	3.55

Table 2 Major and trace elements of garnets analyzed by LA-ICP-MS in granite and pegmatite from the Gangdese orogen.

Grain	12LS257-G1					12LS257-G2				
Spot	101	102	103	104	105	201	202	203	204	205
Major elements (wt.%)										
SiO_2	40.2	39.6	39.3	39.5	39.7	39.9	39.7	39.5	39.3	39.1
TiO_2	0.051	0.17	0.17	0.063	0.046	0.048	0.059	0.14	0.20	0.046
Al_2O_3	18.3	18.0	18.2	18.7	18.8	18.3	18.7	18.5	18.2	18.9
FeO	18.6	18.7	18.7	18.4	18.3	18.7	18.1	18.0	18.2	18.1
MnO	19.6	19.7	19.8	20.1	19.9	19.8	20.0	20.2	20.5	20.4
MgO	1.07	1.11	1.14	1.14	1.07	1.08	1.14	1.15	1.15	1.10
CaO	1.34	1.46	1.53	1.40	1.40	1.39	1.39	1.47	1.45	1.57
Na_2O	0.027	0.053	0.036	0.022	0.020	0.021	0.029	0.042	0.036	0.017
P_2O_5	0.012	0.057	0.065	0.024	0.014	0.014	0.012	0.040	0.050	0.014
Total	99.20	98.84	99.00	99.33	99.28	99.29	99.20	99.10	99.00	99.33
Trace elements (ppm)										
Sc	38.2	22.3	21.3	16.4	38.9	40.6	26.6	16.5	21.0	40.0
V	17.6	5.70	5.67	8.75	15.4	15.8	14.3	10.6	10.2	12.7
Cr	1.14	b.d	b.d	0.34	0.18	0.75	1.61	3.52	0.0000	2.29
Sr	0.30	0.22	0.099	0.033	0.13	0.093	0.19	0.066	0.17	0.22
Y	932	3120	2384	701	754	760	1172	1951	2410	650
Zr	2.69	20.9	23.7	4.84	2.31	2.53	3.58	8.95	20.1	2.81
Nb	b.d	6.53	8.60	0.024	0.003	b.d	b.d	0.30	4.02	0.019
Pb	0.001	0.008	0.015	0.009	b.d	0.004	0.048	0.012	0.054	0.149
Th	0.003	0.005	0.008	b.d	b.d	0.005	b.d.	b.d.	0.044	0.002
U	0.014	2.47	2.45	0.037	0.026	0.031	0.021	0.21	1.46	0.027
La	0.002	b.d.	b.d.	0.002	0.009	0.002	b.d	b.d	b.d	0.008
Ce	0.009	0.039	0.062	b.d	0.002	b.d	0.009	0.030	0.059	0.010
Pr	0.004	0.045	0.054	0.001	0.006	0.002	b.d	0.024	0.051	0.005
Nd	0.034	0.97	1.26	0.20	0.11	0.059	0.12	0.94	1.25	0.053
Sm	0.41	9.42	13.5	2.49	0.76	0.52	1.13	9.33	10.9	0.79
Eu	0.25	1.00	1.57	0.60	0.15	0.15	0.28	1.00	1.08	0.17
Gd	9.12	70.7	81.2	24.5	8.50	9.16	15.0	59.3	68.6	9.44
Tb	5.92	38.3	40.8	11.1	5.05	5.61	9.10	26.5	33.0	5.49
Dy	97.4	391	341	102	79.1	82.1	133	248	314	74.2
Ho	43.2	88.5	59.5	21.2	31.7	31.1	47.2	54.5	67.8	24.1
Er	221	284	157	65.2	146	130	201	164	205	98.5
Tm	54.7	57.3	27.5	12.4	32.4	26.6	46.2	28.9	38.7	22.0
Yb	599	519	216	112	315	237	458	226	313	220
Lu	124	68.9	24.9	15.5	58.6	40.7	73.0	28.4	38.2	39.4
$(Yb/Gd)_N$	79	8.9	3.2	5.5	45	31	37	4.6	5.5	28

Grain	12LS257-G3					12LS258-G1			
Spot	301	302	303	304	305	101	102	103	104
Major elements (wt.%)									
SiO_2	40.0	39.7	39.3	39.3	39.4	35.8	36.0	35.8	35.7
TiO_2	0.045	0.054	0.076	0.048	0.041	0.062	0.045	0.055	0.170
Al_2O_3	18.4	18.5	18.6	18.7	18.8	21.2	21.2	20.9	20.6
FeO	18.2	18.5	18.6	18.6	18.4	18.4	17.7	16.0	17.0
MnO	20.1	19.9	19.9	20.0	20.0	21.4	23.0	24.8	23.4
MgO	1.04	1.13	1.14	1.12	1.07	1.12	1.11	1.00	1.05
CaO	1.40	1.41	1.48	1.49	1.57	1.63	1.18	1.32	1.60
Na_2O	0.018	0.022	0.032	0.021	0.016	0.036	0.016	0.014	0.034
P_2O_5	0.011	0.015	0.017	0.014	0.0070	0.027	0.036	0.040	0.055
Total	99.30	99.22	99.16	99.25	99.29	99.65	99.90	99.89	99.64
Trace elements (ppm)									
Sc	37.3	36.0	20.5	30.8	44.9	24.8	5.38	4.70	18.5
V	15.4	17.1	16.0	13.1	14.0	9.46	1.01	1.30	2.36
Cr	1.71	1.70	1.08	1.34	0.088	2.45	b.d.	3.22	b.d.
Sr	0.11	0.29	0.16	0.14	0.12	0.16	0.060	0.061	0.18
Y	704	787	1446	851	753	1785	416	467	1845
Zr	1.96	2.20	4.15	2.95	1.12	5.62	8.51	9.64	23.5
Nb	0.0017	b.d	0.021	b.d	b.d	0.018	0.070	0.14	5.24
Pb	b.d	0.013	0.029	0.030	b.d	0.084	0.674	0.029	0.050
Th	0.016	0.002	0.009	0.004	b.d	b.d.	0.023	b.d.	b.d.
U	0.009	0.011	0.049	0.032	b.d	0.019	0.072	0.11	0.63
La	b.d	0.005	0.008	b.d	b.d	0.007	0.014	b.d.	b.d.
Ce	0.0078	b.d	0.002	0.003	b.d	0.009	0.16	0.030	b.d.
Pr	0.013	b.d	0.008	0.003	0.005	0.020	0.014	0.020	0.11
Nd	0.092	0.057	0.38	b.d	0.15	0.68	0.24	0.37	1.45
Sm	0.51	0.54	2.49	0.61	0.75	4.93	7.58	10.0	12.0
Eu	0.23	0.16	0.51	0.20	0.12	0.76	0.57	0.73	1.21
Gd	7.37	8.63	28.1	11.5	8.97	41.7	54.7	55.7	72.5
Tb	4.77	5.54	15.4	6.83	5.53	18.6	16.9	17.3	29.9
Dy	75.2	85.6	191	98.9	83.0	216	94.9	101	273
Ho	29.8	38.3	52.2	37.6	30.6	56.8	8.27	10.5	50.6
Er	129	202	173	166	129	158	9.96	13.4	126
Tm	28.8	52.6	35.7	37.1	28.1	32.6	1.02	1.51	25.6
Yb	268	607	334	381	272	215	4.91	6.74	161
Lu	49.0	140	44.2	61.7	46.8	26.4	0.44	0.53	19.3
$(Yb/Gd)_N$	44	85	14	40	37	6.2	0.1	0.1	2.7

Table 2 (Continued)

Grain	12LS258-G1			12LS258-G2								12LS258-G3							
Spot	105	106	107	201	202	203	204	205	206	207	208	301	302	303	304	305	306	307	308
Major elements (wt.%)																			
SiO_2	35.6	35.8	35.5	35.6	35.5	37.7	35.4	35.1	35.2	35.8	39.1	35.8	35.6	35.5	35.5	35.2	35.6	35.4	35.2
TiO_2	0.120	0.120	0.061	0.042	0.0709	0.039	0.088	0.084	0.090	0.050	0.050	0.042	0.060	0.030	0.071	0.180	0.055	0.050	0.055
Al_2O_3	20.6	20.6	20.7	21.4	21.4	20.2	20.8	20.9	20.9	21.3	20.4	21.6	21.5	21.6	21.5	21.4	21.7	22.0	21.8
FeO	17.6	18.5	18.6	17.8	16.1	15.4	16.3	16.2	16.4	16.5	16.4	18.5	18.5	17.0	15.6	16.1	17.1	18.1	18.0
MnO	23.3	22.3	22.2	22.4	24.3	24.4	24.6	25.1	24.7	23.8	21.1	20.8	21.4	23.5	24.6	24.2	23.1	21.9	21.8
MgO	1.07	1.07	0.94	1.05	0.99	0.89	0.98	0.97	0.99	1.04	0.97	1.16	1.05	1.07	0.99	1.01	1.09	1.12	1.02
CaO	1.46	1.44	1.59	1.38	1.18	1.13	1.41	1.41	1.40	1.11	1.52	1.60	1.49	1.24	1.52	1.66	1.28	1.24	1.56
Na_2O	0.028	0.025	0.031	0.027	0.035	0.027	0.032	0.019	0.023	0.025	0.057	0.039	0.042	0.010	0.010	0.011	0.016	0.020	0.042
P_2O_5	0.051	0.037	0.028	0.028	0.051	0.035	0.055	0.066	0.074	0.038	0.028	0.026	0.028	0.030	0.042	0.050	0.040	0.035	0.027
Total	99.78	99.83	99.67	99.68	99.71	99.81	99.72	99.86	99.80	99.78	99.73	99.53	99.55	99.92	99.93	99.75	99.88	99.84	99.50
Trace elements (ppm)																			
Sc	23.3	21.4	22.6	18.8	11.1	6.00	9.45	12.3	10.6	6.64	23.2	22.0	23.0	5.65	4.86	18.3	9.07	11.4	23.0
V	2.65	2.73	8.96	6.67	2.02	0.81	1.91	2.04	1.76	2.04	7.17	5.76	8.75	0.58	0.72	3.03	0.80	1.46	7.95
Cr	b.d.	b.d.	1.75	0.70	0.92	2.99	b.d.	2.32	8.30	1.48	1.90	b.d.	1.30	b.d.	0.51	b.d.	1.70	1.79	b.d.
Sr	0.10	0.16	0.24	0.20	0.26	b.d.	0.19	0.12	0.34	0.20	0.82	0.24	0.38	0.039	0.020	0.095	0.0068	0.086	0.46
Y	1085	822	1725	1396	1406	971	1423	562	862	1111	1273	2244	2221	321	231	1155	511	728	2325
Zr	20.2	14.1	8.07	6.02	14.7	6.15	27.4	42.9	60.1	10.7	3.31	5.70	6.09	6.06	13.3	22.7	9.74	9.15	6.54
Nb	4.68	0.81	0.011	0.015	1.47	0.050	1.04	3.97	6.16	0.11	0.24	0.027	0.12	b.d.	0.36	7.37	0.37	0.098	0.018
Pb	1.957	0.640	0.022	0.031	1.384	1.038	2.685	1.721	3.761	2.257	16.6	0.037	4.579	b.d.	b.d.	0.514	0.013	b.d.	2.858
Th	0.067	0.030	0.007	b.d.	0.10	0.074	0.42	0.26	0.41	0.18	0.48	b.d.	0.37	b.d.	0.020	0.067	b.d.	0.019	0.039
U	0.35	0.25	0.018	0.023	0.36	0.050	0.26	0.62	1.17	0.017	0.045	0.007	0.007	0.026	0.26	0.58	0.099	0.056	0.026
La	0.007	0.012	b.d.	b.d.	0.042	b.d.	0.065	0.006	b.d.	0.007	0.021	b.d.	b.d.	0.016	b.d.	0.017	b.d.	b.d.	0.009
Ce	0.24	0.14	0.071	0.006	0.057	0.091	0.57	0.39	0.85	0.16	2.12	0.015	0.79	b.d.	0.070	0.17	0.024	0.015	0.055
Pr	0.040	0.027	0.009	0.010	0.010	0.026	0.062	0.043	0.11	0.005	0.057	0.012	0.015	0.006	0.050	0.056	0.038	0.010	0.019
Nd	0.78	0.83	0.26	0.032	0.44	0.32	0.88	1.54	2.65	0.26	0.45	0.056	0.47	0.28	1.64	1.64	0.47	0.52	0.17
Sm	8.63	7.18	3.26	2.42	7.91	4.67	10.4	11.5	17.0	5.04	2.63	2.79	2.26	8.03	10.7	14.0	6.29	6.44	2.13
Eu	0.86	0.92	0.54	0.25	0.57	0.32	1.00	1.10	1.23	0.37	0.47	0.41	0.50	0.63	1.47	1.13	0.88	0.48	0.36
Gd	53.8	37.1	32.1	27.7	52.9	40.5	65.3	60.7	78.4	52.9	28.8	31.0	31.5	47.2	32.6	60.1	32.0	48.8	28.8
Tb	19.3	13.7	16.7	13.0	22.5	19.3	25.8	18.7	23.3	22.9	13.9	17.2	17.1	13.4	7.52	21.1	11.5	16.7	16.2
Dy	164	119	209	178	199	157	217	110	157	200	160	254	242	67.5	43.8	179	87.1	119	251
Ho	27.4	21.1	54.2	57.7	37.1	22.7	35.2	12.6	20.2	29.7	46.5	86.5	78.4	6.14	5.78	32.6	13.1	18.2	91.4
Er	57.3	49.2	155	215	97.1	38.6	71.1	18.0	34.9	55.3	141	317	267	8.35	10.5	82.6	26.0	44.6	333
Tm	11.9	10.1	31.2	51.9	22.5	5.49	13.0	2.61	5.45	9.48	29.7	71.7	59.1	1.61	1.64	19.4	4.86	9.24	79.9
Yb	68.0	65.7	203	374	160	27.8	74.5	11.6	30.9	57.5	201	482	389	7.62	9.60	126	30.1	61.6	579
Lu	7.37	7.52	23.6	67.4	24.3	2.70	8.22	1.24	3.21	6.53	31.4	75.2	55.1	0.77	0.86	17.0	3.49	8.68	88.8
$(Yb/Gd)_N$	1.5	2.1	7.7	16	3.7	0.8	1.4	0.2	0.5	1.3	8.4	19	15	0.2	0.4	2.5	1.1	1.5	24

Table 3 Zircon U-Pb isotope data for granite and pegmatite from the Gangdese orogen.

Analysis No	Element Pb (ppm)	Th (ppm)	U (ppm)	Th/U	Isotope ratio $^{207}Pb/^{206}Pb$	2σ	$^{207}Pb/^{235}U$	2σ	$^{206}Pb/^{238}U$	2σ	$^{208}Pb/^{232}Th$	2σ	Apparent age (Ma) $^{207}Pb/^{206}Pb$	2σ	$^{207}Pb/^{235}U$	2σ	$^{206}Pb/^{238}U$	2σ	$^{208}Pb/^{232}Th$	2σ
12LS257																				
1	74.4	1759	5452	0.32	0.0445	0.0013	0.0765	0.0021	0.0124	0.0001	0.0040	0.0001	error	error	74.8	1.9	79.3	0.6	80.3	1.5
2	17.38	72.6	342	0.21	0.0533	0.0017	0.3538	0.0116	0.0479	0.0008	0.0159	0.0005	343	39.8	308	8.7	302	5.1	319	10.
3	10.42	253	767	0.33	0.0455	0.0018	0.0787	0.0031	0.0125	0.0002	0.0038	0.0001	error		76.9	2.9	80.2	1.0	76.8	2.2
4	7.41	58.1	542	0.11	0.0518	0.0041	0.0922	0.0069	0.0130	0.0002	0.0045	0.0003	276	184	89.6	6.4	83.5	1.1	90.3	6.3
5	31.58	103	508	0.20	0.0530	0.0014	0.4240	0.0110	0.0578	0.0006	0.0188	0.0005	328	26.9	359	7.9	363	3.4	376	9.9
6	93.5	2664	6615	0.40	0.0472	0.0008	0.0826	0.0017	0.0126	0.0001	0.0038	0.0001	57.5	40.7	80.6	1.6	80.9	0.9	77.6	1.6
7	39.54	115	3190	0.04	0.0478	0.0011	0.0799	0.0019	0.0121	0.0001	0.0084	0.0037	100	53.7	78.1	1.7	77.6	0.6	169	75.
8	55.3	371	817	0.45	0.0529	0.0011	0.4387	0.0091	0.0605	0.0009	0.0185	0.0004	324	46.3	369	6.4	378	5.6	371	7.4
9	21.74	709	1584	0.45	0.0477	0.0017	0.0796	0.0028	0.0122	0.0002	0.0039	0.0001	83.4	81.5	77.7	2.6	78.2	1.2	78.4	2.6
10	52.78	186	894	0.21	0.0534	0.0010	0.3971	0.0086	0.0538	0.0006	0.0164	0.0004	346	42.6	340	6.3	338	3.4	329	8.9
11	25.70	316	1825	0.17	0.0482	0.0013	0.0866	0.0024	0.0131	0.0001	0.0049	0.0003	106	67	84.3	2.3	83.9	0.7	97.9	5.3
12	18.21	293	1361	0.21	0.0462	0.0013	0.0795	0.0024	0.0124	0.0001	0.0039	0.0001	9.4	66.7	77.7	2.2	79.7	0.6	79.5	2.4
13	78.9	2031	5623	0.36	0.0504	0.0010	0.0871	0.0018	0.0126	0.0001	0.0045	0.0001	213	46.3	84.8	1.7	80.4	0.9	90.9	2.0
14	7.30	273	496	0.55	0.0466	0.0024	0.0798	0.0040	0.0125	0.0002	0.0038	0.0001	27.9	119	77.9	3.8	80.1	1.0	77.2	2.8
15	22.26	387	1650	0.23	0.0490	0.0013	0.0842	0.0024	0.0125	0.0001	0.0041	0.0001	146	64.8	82.1	2.3	79.8	0.7	83.2	2.2
16	60.47	959	4535	0.21	0.0495	0.0010	0.0848	0.0018	0.0124	0.0001	0.0042	0.0001	172	50.0	82.6	1.7	79.7	0.8	84.1	2.3
17	88.3	2693	6223	0.43	0.0490	0.0010	0.0833	0.0016	0.0123	0.0001	0.0039	0.0001	150	46.3	81.3	1.5	79.1	0.7	79.6	1.4
18	17.08	559	1197	0.47	0.0484	0.0013	0.0815	0.0022	0.0123	0.0001	0.0043	0.0001	120	64.8	79.5	2.0	78.5	0.9	86.0	2.1
19	7.39	247	519	0.48	0.0472	0.0023	0.0800	0.0038	0.0123	0.0001	0.0037	0.0001	57.5	111	78.1	3.6	79.0	0.8	74.8	2.6
20	5.09	166	369	0.45	0.0503	0.0033	0.0837	0.0056	0.0120	0.0002	0.0038	0.0001	209	149	81.7	5.3	76.9	1.1	76.2	2.7
21	14.22	265	1088	0.24	0.0522	0.0015	0.0864	0.0024	0.0120	0.0001	0.0041	0.0001	295	66.7	84.2	2.2	76.8	0.8	82.8	2.8
22	10.78	336	732	0.46	0.0493	0.0018	0.0855	0.0032	0.0126	0.0001	0.0042	0.0001	161	85	83.3	3.0	80.5	0.8	84.2	2.4
23	34.56	352	1561	0.23	0.0498	0.0011	0.1427	0.0034	0.0209	0.0003	0.0081	0.0003	183	51.8	135	3.0	133	2.1	163	6.4
24	43.81	1243	3129	0.40	0.0482	0.0010	0.0826	0.0018	0.0124	0.0001	0.0039	0.0001	109	51.8	80.6	1.7	79.4	0.7	78.8	1.4
25	39.8	1975	2572	0.77	0.0467	0.0012	0.0802	0.0021	0.0124	0.0001	0.0040	0.0001	35.3	64.8	78.3	2.0	79.3	0.6	81.1	1.5
26	51.86	138	1369	0.10	0.0510	0.0010	0.2544	0.0050	0.0360	0.0003	0.0104	0.0003	243	46.3	230	4.0	228	1.8	210	6.0

Table 3 (Continued)

Analysis No	Element Pb (ppm)	Th (ppm)	U (ppm)	Th/U	Isotope ratio $^{207}Pb/^{206}Pb$	2σ	$^{207}Pb/^{235}U$	2σ	$^{206}Pb/^{238}U$	2σ	$^{208}Pb/^{232}Th$	2σ	Apparent age (Ma) $^{207}Pb/^{206}Pb$	2σ	$^{207}Pb/^{235}U$	2σ	$^{206}Pb/^{238}U$	2σ	$^{208}Pb/^{232}Th$	2σ
27	11.53	343	809	0.42	0.0490	0.0017	0.0846	0.0029	0.0125	0.0001	0.0040	0.0001	150	75.0	82.4	2.8	79.8	0.9	80.9	2.1
28	18.17	492	1289	0.38	0.0452	0.0015	0.0768	0.0022	0.0124	0.0002	0.0039	0.0001	error		75.1	2.1	79.3	1.0	78.1	2.1
29	18.30	92.1	293	0.31	0.0511	0.0014	0.3930	0.0106	0.0554	0.0006	0.0180	0.0005	256	63.0	337	7.7	347	3.9	360	9.7
30	24.55	725	1718	0.42	0.0478	0.0019	0.0824	0.0035	0.0123	0.0002	0.0039	0.0001	87	102	80.4	3.3	79.0	1.0	79.3	2.1
31	80.2	4024	5089	0.79	0.0461	0.0009	0.0798	0.0017	0.0125	0.0002	0.0040	0.0001	400	-344	77.9	1.6	79.8	1.2	81.7	1.6
32	41.0	1996	2716	0.74	0.0471	0.0011	0.0776	0.0017	0.0119	0.0001	0.0038	0.0001	50.1	56	75.9	1.6	76.1	0.8	77.1	1.5
33	7.27	127	439	0.29	0.0454	0.0019	0.0897	0.0036	0.0144	0.0002	0.0048	0.0002	error		87.2	3.4	91.9	1.5	97.7	3.8
34	34.68	690	2537	0.27	0.0477	0.0010	0.0821	0.0018	0.0124	0.0002	0.0040	0.0001	83.4	84.2	80.1	1.6	79.7	1.0	81.3	1.9
35	3.81	96.9	267	0.36	0.0460	0.0027	0.0771	0.0042	0.0123	0.0002	0.0039	0.0002	error		75.4	4.0	78.8	1.3	78.4	4.0
36	77.0	4987	4496	1.11	0.0470	0.0010	0.0805	0.0017	0.0124	0.0001	0.0039	0.0001	55.7	42.6	78.6	1.6	79.2	0.6	78.5	1.2
37	65.0	1843	3935	0.47	0.0470	0.0010	0.0925	0.0020	0.0143	0.0002	0.0049	0.0001	55.7	46.3	89.9	1.9	91.5	1.3	98.6	2.0
12LS258																				
1	289	686	24163	0.03	0.0496	0.0008	0.0824	0.0015	0.0120	0.0001	0.0042	0.0001	176	6.5	80.4	1.4	76.9	0.8	85.5	2.3
2	372	994	30782	0.03	0.0503	0.0008	0.0830	0.0017	0.0119	0.0001	0.0050	0.0003	209	43.5	81.0	1.6	76.3	0.8	102	6.1
3	407	1050	33350	0.03	0.0498	0.0007	0.0820	0.0013	0.0119	0.0001	0.0048	0.0002	183	35.2	80.0	1.2	76.5	0.8	95.9	3.5
4	634	1691	52154	0.03	0.0501	0.0008	0.0823	0.0015	0.0119	0.0001	0.0048	0.0002	211	37.0	80.3	1.4	76.2	0.9	97.2	3.1
5	244	409	20168	0.02	0.0473	0.0008	0.0783	0.0014	0.0120	0.0001	0.0043	0.0001	64.9	42.6	76.5	1.4	76.8	0.6	87.6	2.8
6	293	705	24363	0.03	0.0520	0.0009	0.0863	0.0017	0.0120	0.0001	0.0086	0.0006	287	36	84.1	1.6	76.7	0.7	174	11.0
7	233	401	19162	0.02	0.0479	0.0007	0.0792	0.0013	0.0119	0.0001	0.0040	0.0001	98.2	35.18	77.4	1.2	76.6	0.6	79.9	2.24
9	342	774	28098	0.03	0.0512	0.0009	0.0845	0.0020	0.0119	0.0001	0.0083	0.0007	250	45	82.3	1.9	76.0	0.9	167	13.6
10	352	650	28635	0.02	0.0471	0.0009	0.0781	0.0015	0.0120	0.0001	0.0039	0.0001	53.8	44.4	76.3	1.4	76.7	0.7	77.9	2.0
12	343	550	27991	0.02	0.0471	0.0008	0.0779	0.0014	0.0119	0.0001	0.0039	0.0001	57.5	38.9	76.2	1.3	76.4	0.7	79.2	2.1
13	283	557	23077	0.02	0.0470	0.0007	0.0780	0.0015	0.0120	0.0001	0.0042	0.0001	55.7	37.0	76.3	1.4	76.8	0.8	84.2	2.3
14	311	692	25200	0.03	0.0538	0.0011	0.0878	0.0021	0.0117	0.0001	0.0117	0.0009	365	44.4	85.5	1.9	75.2	0.7	235	17.9
15	346	897	27180	0.03	0.0498	0.0010	0.0842	0.0017	0.0122	0.0001	0.0063	0.0004	183	15.7	82.1	1.6	78.3	0.6	126	8.9
16	241	637	19777	0.03	0.0477	0.0007	0.0792	0.0014	0.0120	0.0001	0.0039	0.0001	87	35.2	77.4	1.3	76.8	0.8	77.7	2.2
17	211	360	17272	0.02	0.0483	0.0009	0.0807	0.0017	0.0121	0.0001	0.0040	0.0001	117	41.7	78.8	1.6	77.4	0.9	80.7	2.7

Table 4 Trace elements for zircon in granite and pegmatite from the Gangdese orogen

Sample	12LS257																			
Spot	1	2	3	4	5	6	7	8	9	10	11	12	13	14	15	16	17	18	19	20
La	0.013	0.008	0.004	0.17	0.019	0.029	1.09	0.34	0.008	0.038	0.009	-	0.027	0.045	-	0.059	0.010	0.002	0.004	0.021
Ce	47.7	2.20	33.7	9.54	1.78	48.5	5.31	6.83	66.2	3.80	23.6	28.0	57.3	32.8	24.8	33.0	53.9	42.4	29.9	17.0
Pr	0.038	0.046	0.057	0.080	0.043	0.078	0.024	0.27	0.100	0.057	0.040	0.043	0.099	0.089	0.015	0.048	0.076	0.047	0.057	0.030
Nd	1.12	0.75	1.37	0.37	0.93	1.52	0.77	3.26	1.40	1.33	0.93	1.40	1.79	1.46	0.43	0.88	1.85	1.20	0.95	1.28
Sm	6.42	2.36	4.49	1.34	3.48	7.66	1.93	7.54	7.35	4.40	4.47	5.58	8.58	4.79	2.99	4.50	9.05	4.70	3.14	3.18
Eu	1.95	0.10	1.84	0.70	0.11	2.42	0.46	0.23	1.50	0.36	1.31	2.11	2.96	2.07	1.59	1.40	2.74	2.73	1.93	1.56
Gd	61.8	18.9	45.6	9.75	28.2	73.1	20.9	53.4	71.6	34.7	46.8	55.5	86.3	39.5	35.6	45.0	76.9	47.0	30.8	22.0
Tb	27.6	7.88	20.2	3.96	11.9	30.9	12.1	21.6	29.5	15.4	22.3	26.7	38.3	15.2	17.2	21.2	32.3	18.7	12.3	8.26
Dy	396	101	287	58.8	160	429	199	294	405	207	328	394	524	206	254	322	436	255	165	109
Ho	167	41.4	119	27.2	66.2	174	88.7	119	161	85.9	138	166	214	85.3	112	144	173	103	70.5	45.6
Er	784	196	555	140	314	806	477	544	750	411	669	790	991	405	551	729	791	483	334	222
Tm	175	43.0	120	33.4	66.8	176	125	115	164	90.0	153	176	218	88.8	123	171	170	104	74.3	50.1
Yb	1675	404	1159	354	625	1656	1348	1005	1537	839	1490	1669	2050	853	1204	1663	1570	987	713	491
Lu	322	81.5	221	79.6	126	319	281	190	296	170	287	317	401	177	245	339	303	201	149	108
MREE	493	130	359	75	203	543	235	377	515	262	403	483	660	268	312	394	557	328	213	144
HREE	3122	767	2173	634	1199	3131	2320	1973	2909	1596	2737	3117	3874	1609	2236	3045	3006	1878	1341	917
Ce/Ce*	342.4	13.9	179.1	19.8	11.0	167.2	3.6	5.3	200.2	16.3	169.7	200.1	161.6	95.4	501.9	142.5	210.7	275.0	158.1	136.0
Eu/Eu*	0.20	0.03	0.25	0.43	0.02	0.21	0.14	0.03	0.13	0.06	0.18	0.24	0.21	0.32	0.28	0.19	0.22	0.36	0.39	0.42
$(Sm/La)_N$	761	484	1819	12	278	402	3	35	1508	182	788	-	497	166	-	118	1518	3529	1142	233
$(Yb/Sm)_N$	235	154	232	238	162	195	629	120	188	172	300	269	215	160	362	333	156	189	204	139
Y	5167	1235	3704	899	1910	5327	2966	3507	5058	2507	4383	5289	6661	2647	3495	4575	5316	3205	2148	1450
Nb	71.9	1.73	15.5	5.28	1.87	74.2	12.9	2.81	33.2	3.34	21.9	19.8	67.8	6.74	26.5	64.6	65.6	16.7	7.16	2.45
Ta	15.3	1.54	3.33	3.36	1.45	17.7	10.7	1.53	8.32	2.56	7.09	5.78	15.1	1.31	6.08	18.0	15.6	3.17	1.26	0.77
Hf	16508	12659	13387	11906	13166	16009	19190	12630	14115	13608	18540	13629	13992	10656	13766	13164	15694	11970	11107	10996
Ti	5.04	5.83	5.06	3.28	4.61	4.43	1.84	22.6	3.85	2.08	3.27	3.29	7.04	4.25	4.41	3.86	7.06	5.81	5.47	2.72
T_{Ti}(℃)	684	696	684	652	677	674	611	818	663	619	651	652	711	671	674	664	711	695	690	638

Note: T_{Ti} (°C) denotes the Ti-in-zircon temperature following the experimental calibration of Watson et al. (2006).

Sample No.	12LS257															
Spot	21	22	23	24	25	26	27	28	29	30	31	32	33	34	35	36	37
La	-	0.004	3.12	0.014	0.004	0.17	0.016	0.013	0.004	0.009	0.021	0.022	-	0.001	0.051	0.12	0.086
Ce	27.6	31.1	29.9	32.5	52.2	3.31	31.8	45.6	2.66	34.7	98.4	59.3	5.50	41.6	12.2	115	43.6
Pr	0.021	0.032	1.17	0.040	0.086	0.11	0.040	0.051	0.046	0.046	0.17	0.093	0.061	0.050	0.033	0.26	0.075
Nd	0.45	0.82	8.55	1.17	1.94	0.73	0.89	1.14	1.14	0.98	3.70	1.93	0.57	1.60	0.56	6.06	3.16
Sm	2.75	3.92	8.00	4.40	7.88	1.11	4.19	4.75	2.89	4.91	13.7	7.81	1.05	7.45	1.93	17.4	5.64
Eu	1.25	1.14	1.68	1.74	3.46	0.41	0.99	1.26	0.13	2.43	5.90	4.25	0.55	2.52	1.03	7.65	2.08
Gd	30.7	36.0	50.3	36.0	58.0	7.37	33.3	38.9	19.3	45.2	101	59.8	6.52	74.4	13.6	112	48.8
Tb	13.8	13.9	19.3	15.2	21.0	3.55	14.1	16.2	7.77	19.1	37.4	21.8	2.43	33.4	5.41	39.7	21.3
Dy	207	187	253	204	267	57.0	194	229	97.7	270	464	271	32.3	477	76.5	471	285
Ho	88.5	76.1	102	84.1	103	26.6	79.9	92.7	38.4	110	178	105	14.2	193	33.7	173	111
Er	436	364	483	402	461	150	387	450	181	526	790	471	74.8	891	171	736	493
Tm	100	81.2	105	89.6	95.3	38.1	86.7	99.6	37.8	114	164	101	18.2	192	40.5	151	105
Yb	1009	787	1009	874	880	415	845	983	357	1088	1516	947	201	1793	431	1384	959
Lu	209	158	201	177	171	95.2	170	192	71.5	218	298	193	49.0	337	100	272	190
MREE	256	242	332	262	357	69	247	290	128	342	622	364	43	595	98	648	363
HREE	1843	1466	1901	1626	1710	724	1569	1817	685	2056	2945	1817	357	3405	776	2716	1858
Ce/Ce*	411.6	283.7	3.8	219.6	185.2	5.8	215.4	250.2	17.4	215.0	171.3	180.8	27.9	259.0	71.3	116.1	124.2
Eu/Eu*	0.26	0.20	0.19	0.29	0.36	0.33	0.18	0.20	0.04	0.33	0.35	0.43	0.49	0.21	0.45	0.40	0.26
$(Sm/La)_N$	-	1401	4	476	2742	10	411	567	1074	814	998	542	-	24555	59	226	102
$(Yb/Sm)_N$	330	181	113	179	101	337	181	186	111	199	99	109	172	217	201	72	153
Y	2851	2382	3098	2602	3099	857	2553	2945	1151	3384	5370	3196	469	5956	1084	5172	3351
Nb	20.1	6.77	10.4	30.3	32.5	4.69	6.64	18.6	1.86	25.3	61.0	27.0	0.53	38.9	3.08	48.6	47.2
Ta	4.88	2.12	5.27	9.49	5.51	6.29	2.17	6.13	1.14	4.83	10.00	4.87	0.46	8.51	0.73	8.14	8.12
Hf	12991	13259	12733	14158	13017	16783	13221	15074	11410	12515	11524	11314	11423	15945	9947	10978	12986
Ti	3.07	2.85	4.61	25.7	6.80	25.1	2.24	2.55	7.53	4.95	9.73	5.34	4.78	12.4	3.40	10.8	10.8
T_{Ti}(℃)	647	641	677	831	708	829	625	634	716	683	738	688	680	760	654	747	747

Table 4 (Continued)

Note: T_{Ti} (°C) denotes the Ti-in-zircon temperature following the experimental calibration of Watson et al. (2006).

Table 4 (Continued)

Sample No.	12LS258													
Spot	1	2	3	4	5	6	7	9	10	12	13	14	15	17
La	1.13	2.62	0.69	7.15	0.066	0.67	0.041	2.15	0.103	0.0165	0.096	0.47	0.150	0.147
Ce	9.54	9.81	10.08	24.4	5.96	8.56	5.30	7.70	8.72	9.57	6.75	8.31	10.06	4.97
Pr	0.70	0.64	0.55	3.87	0.052	0.378	0.051	0.88	0.091	0.0261	0.071	0.205	0.079	0.075
Nd	5.71	4.46	5.07	20.5	1.11	3.61	0.79	5.98	1.17	0.75	1.43	2.04	2.13	1.11
Sm	18.28	21.78	24.71	62.5	11.88	17.27	10.53	26.16	11.33	11.88	15.59	16.43	20.64	9.10
Eu	2.93	2.18	3.24	5.76	1.07	2.15	0.97	3.01	1.08	0.85	1.24	1.47	1.84	0.98
Gd	185.1	242.0	241.7	458	148.8	170.9	133.0	241.7	114.9	116.0	179.5	178.2	215.9	111.3
Tb	88.4	118.1	114.7	186.1	72.8	86.9	66.9	119.3	55.0	58.6	91.3	88.3	110.7	55.9
Dy	832	1099	1079	1169	690	818	605	1075	506	537	826	834	1080	525
Ho	161.1	214.1	209.5	141.1	136.8	161.1	117.2	201.6	96.5	103.8	159.0	164.7	224.4	108.6
Er	405	517	503	248	361	407	300	478	236	253	398	408	583	317
Tm	61.1	76.8	75.0	32.50	58.8	63.0	48.8	73.0	34.8	37.6	62.5	61.6	90.5	56.5
Yb	432	526	515	213.4	441	444	365	517	247.9	260.9	454	427	623	482
Lu	58.4	68.6	65.7	25.86	67.4	57.1	56.8	65.9	31.74	33.70	59.9	55.7	76.7	73.4
MREE	1127	1483	1463	1881	924	1095	816	1465	688	724	1114	1118	1429	703
HREE	1117	1402	1368	661	1065	1132	888	1336	646	689	1134	1117	1597	1037
Ce/Ce*	2.6	1.8	3.8	1.1	23.4	4.1	24.3	1.4	20.5	90.9	19.2	6.6	22.4	11.5
Eu/Eu*	0.10	0.06	0.08	0.08	0.05	0.08	0.05	0.08	0.06	0.05	0.04	0.05	0.05	0.06
$(Sm/La)_N$	21	22	19	3	33	23	31	18	20	20	26	23	27	48
$(Yb/Sm)_N$	25	13	56	14	277	40	401	19	170	1112	253	55	213	96
Y	7370	9738	9426	8416	6335	7519	5426	9881	4474	4850	7481	7604	10074	4908
Nb	10.76	13.10	11.13	50.9	12.26	18.01	10.19	15.36	32.00	41.9	12.99	12.22	13.07	13.67
Ta	9.63	10.44	9.57	89.4	11.42	10.31	10.99	11.68	32.55	37.9	10.02	9.44	9.84	13.33
Hf	33041	31975	32079	60910	37309	31145	38878	32047	36844	36755	33374	32864	29226	37365
Ti	60	6.0	1.89	21.8	23.0	119	1.29	9.7	0.56	0.60	1.64	3.63	3.33	7.0
T_{Ti}(℃)	927	698	613	814	820	1018	588	738	538	542	604	659	653	711

Note: T_{Ti} (°C) denotes the Ti-in-zircon temperature following the experimental calibration of Watson et al. (2006).

Table 5 Zircon Lu-Hf isotope and oxygen isotope data for granite and pegmatite from the Gangdese orogen

No.	$^{176}Yb/^{177}Hf$	$^{176}Lu/^{177}Hf$	$^{176}Hf/^{177}Hf$	±(2σ)	$t_{6/8}$(Ma)	$(^{176}Hf/^{177}Hf)_i$	$\varepsilon_{Hf}(t)$	±(2σ)	T_{DM1} (Ma)	±(2σ)	$f_{Lu/Hf}$	T_{DM2} (Ma)	±(2σ)	Concordance	$\delta^{18}O$	±(2σ)
12LS257																
1	0.054217	0.001914	0.282967	0.000012	79.3	0.282939	8.5	0.2	415	17	-0.94	600	27	94%	6.24	0.23
2	0.025067	0.000884	0.282460	0.000020	302	0.282447	-4.6	0.3	1118	27	-0.97	1605	44	98%	9.53	0.28
3	0.052068	0.001972	0.282904	0.000011	80.2	0.282876	6.3	0.2	506	16	-0.94	741	25	95%	6.34	0.32
4	0.026151	0.001044	0.283007	0.000012	83.5	0.282992	10.1	0.2	348	16	-0.97	503	26	92%	6.08	0.21
5	0.056442	0.001951	0.282376	0.000015	363	0.282348	-6.5	0.3	1270	21	-0.94	1770	32	98%	9.78	0.20
6	0.064323	0.002164	0.282899	0.000012	80.9	0.282867	6.1	0.2	517	18	-0.93	754	28	99%	6.41	0.24
7	0.046830	0.001807	0.283012	0.000010	77.6	0.282986	10.1	0.2	347	15	-0.95	497	23	99%	6.63	0.19
8	0.062906	0.002019	0.282451	0.000013	378	0.282422	-3.5	0.2	1164	19	-0.94	1595	30	97%	8.98	0.13
9	0.076758	0.002057	0.283005	0.000011	78.2	0.282975	9.8	0.2	360	16	-0.94	515	25	99%	6.46	0.24
10	0.056458	0.001671	0.282439	0.000012	338	0.282414	-4.7	0.2	1172	17	-0.95	1641	26	99%	9.51	0.25
12	0.089786	0.002729	0.283041	0.000014	79.7	0.283001	11.1	0.2	313	21	-0.92	435	31	97%	6.27	0.26
13	0.092757	0.002798	0.283051	0.000014	80.4	0.283010	11.5	0.3	299	21	-0.92	411	32	94%	5.75	0.25
14	0.068099	0.002134	0.282987	0.000012	80.1	0.282955	9.2	0.2	388	17	-0.94	555	27	97%	6.82	0.20
15	0.066397	0.002050	0.283016	0.000012	79.8	0.282986	10.3	0.2	344	17	-0.94	488	27	97%	6.70	0.14
16	0.089544	0.002848	0.282944	0.000009	79.7	0.282902	7.7	0.2	459	14	-0.91	654	21	96%	6.74	0.18
17	0.070917	0.002186	0.283030	0.000010	79.1	0.282998	10.8	0.2	324	14	-0.93	457	22	97%	6.26	0.23
18	0.064734	0.002604	0.283010	0.000013	78.5	0.282972	10.0	0.2	358	19	-0.92	505	29	98%	7.05	0.14
19	0.064879	0.002001	0.282995	0.000013	79.0	0.282966	9.5	0.2	374	20	-0.94	536	30	98%	7.34	0.21
23	0.056695	0.001753	0.282365	0.000012	133	0.282339	-11.7	0.2	1280	17	-0.95	1922	27	98%	*8.63*	*0.13*
24	0.055159	0.002126	0.282884	0.000012	79.4	0.282853	5.6	0.2	538	17	-0.94	788	26	98%	*6.36*	*0.21*
25	0.070426	0.002430	0.283021	0.000019	79.3	0.282985	10.4	0.3	341	28	-0.93	480	43	98%	*6.55*	*0.18*
26	0.043961	0.001624	0.282470	0.000011	228	0.282446	-5.9	0.2	1125	16	-0.95	1632	25	99%	*6.69*	*0.17*
27	0.055196	0.001678	0.283049	0.000014	79.8	0.283024	11.5	0.2	293	20	-0.95	413	32	96%	6.13	0.18
28	0.060599	0.001844	0.283024	0.000010	79.3	0.282997	10.6	0.2	330	15	-0.94	470	23	94%	6.06	0.14

Table 5 (Continued)

No.	$^{176}Yb/^{177}Hf$	$^{176}Lu/^{177}Hf$	$^{176}Hf/^{177}Hf$	±(2σ)	$t_{6/8}$(Ma)	$(^{176}Hf/^{177}Hf)_i$	$\varepsilon_{Hf}(t)$	±(2σ)	T_{DM1} (Ma)	±(2σ)	$f_{Lu/Hf}$	T_{DM2} (Ma)	±(2σ)	Concordance	$\delta^{18}O$	±(2σ)
12LS257																
29	0.025924	0.000821	0.282446	0.000012	347	0.282434	-4.1	0.2	1135	16	-0.98	1607	26	96%	9.06	0.16
30	0.041050	0.001253	0.283058	0.000015	79.0	0.283039	11.8	0.3	277	22	-0.96	391	35	98%	6.80	0.20
31	0.124955	0.003875	0.283107	0.000014	79.8	0.283050	13.4	0.2	221	21	-0.88	288	31	97%	6.67	0.17
32	0.056687	0.001788	0.283054	0.000011	76.1	0.283028	11.5	0.2	287	16	-0.95	404	25	99%	6.13	0.30
34	0.064244	0.002428	0.282975	0.000014	79.7	0.282940	8.8	0.2	408	20	-0.93	582	31	99%	*7.52*	*0.28*
35	0.042121	0.001534	0.283084	0.000013	78.8	0.283061	12.7	0.2	241	19	-0.95	333	30	95%	6.29	0.25
36	0.102056	0.003719	0.283064	0.000023	79.2	0.283010	11.9	0.4	287	35	-0.89	386	52	99%	6.38	0.20
37	0.071692	0.002600	0.283070	0.000036	91.5	0.283032	12.4	0.6	269	53	-0.92	361	81	98%	6.43	0.25
12LS258																
1	0.018948	0.000456	0.283005	0.000008	76.9	0.282998	9.9	0.1	345	11	-0.99	510	18	95%	5.48	0.23
2	0.022797	0.000449	0.283002	0.000009	76.3	0.282995	9.8	0.2	350	13	-0.99	517	20	94%	5.73	0.21
3	0.032588	0.000617	0.283001	0.000008	76.5	0.282992	9.7	0.1	353	11	-0.98	521	18	95%	5.48	0.22
4	0.007035	0.000154	0.282980	0.000007	76.2	0.282977	9.0	0.1	378	10	-1.00	567	16	94%	5.26	0.30
5	0.016902	0.000468	0.282998	0.000009	76.8	0.282991	9.7	0.2	355	13	-0.99	525	21	99%	5.83	0.18
6	0.021762	0.000468	0.283008	0.000008	76.7	0.283001	10.0	0.1	341	12	-0.99	504	19	90%	5.84	0.20
7	0.017280	0.000431	0.282997	0.000009	76.6	0.282991	9.6	0.2	356	13	-0.99	528	21	98%	5.93	0.18
9	0.014303	0.000303	0.282994	0.000008	76.0	0.282990	9.5	0.1	359	11	-0.99	534	19	92%	5.50	0.18
10	0.007139	0.000152	0.283000	0.000008	94.3	0.282998	10.1	0.1	349	11	-1.00	510	18	99%	5.19	0.21
12	0.006346	0.000142	0.283001	0.000009	76.4	0.282999	9.8	0.2	348	13	-1.00	518	21	99%	5.72	0.18
13	0.013865	0.000292	0.282994	0.000009	76.8	0.282989	9.5	0.2	359	12	-0.99	535	20	99%	5.84	0.19
14	0.014403	0.000348	0.282981	0.000019	75.2	0.282976	9.0	0.3	378	26	-0.99	566	43	87%	6.11	0.23
15	0.015027	0.000383	0.283001	0.000031	78.3	0.282995	9.8	0.6	351	44	-0.99	519	71	95%	5.95	0.25
16	0.155214	0.005564	0.283026	0.000016	76.8	0.282945	10.4	0.3	364	26	-0.83	479	36	99%	6.00	0.15
17	0.010732	0.000308	0.282990	0.000011	77.4	0.282985	9.4	0.2	365	15	-0.99	543	25	98%	5.73	0.23

Figure 1

91°E
92°E
93°E
30°N
29°N
Central Lhasa terrane
Southern Lhasa terrane
Linzhou
Maizhokunggar
Lhasa
Gongbo'gyamda
Nyingchi
Yarlung-Tsangpo suture
Tsedong
Gyaca
Nang
Mainling
12LS257
12LS258
N
0
40km
Granite
Sample location
(b)
(a)
80°
90°
100°
35°
30°
25°
Kunlun terrane
Songpan-Ganze terrane
Qiangtang terrane
Lhasa terrane
Himalaya
India continent
Ganite
Linzizong volcanic successions

Figure 2

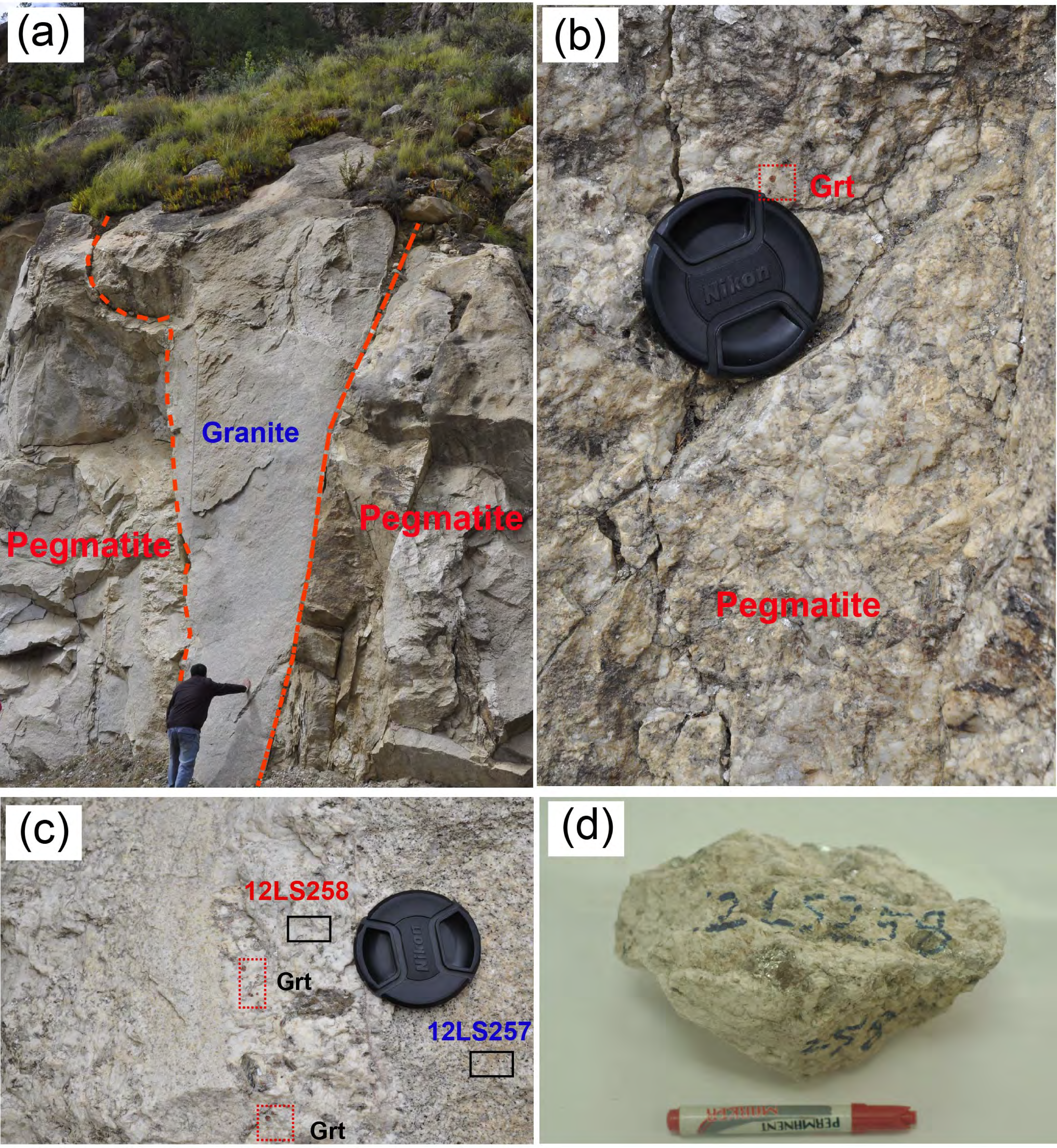
(a)
Granite
Pegmatite
Pegmatite
(b)
Grt
Nikon
Pegmatite
(c)
12LS258
Grt
12LS257
Grt
(d)

Figure 3

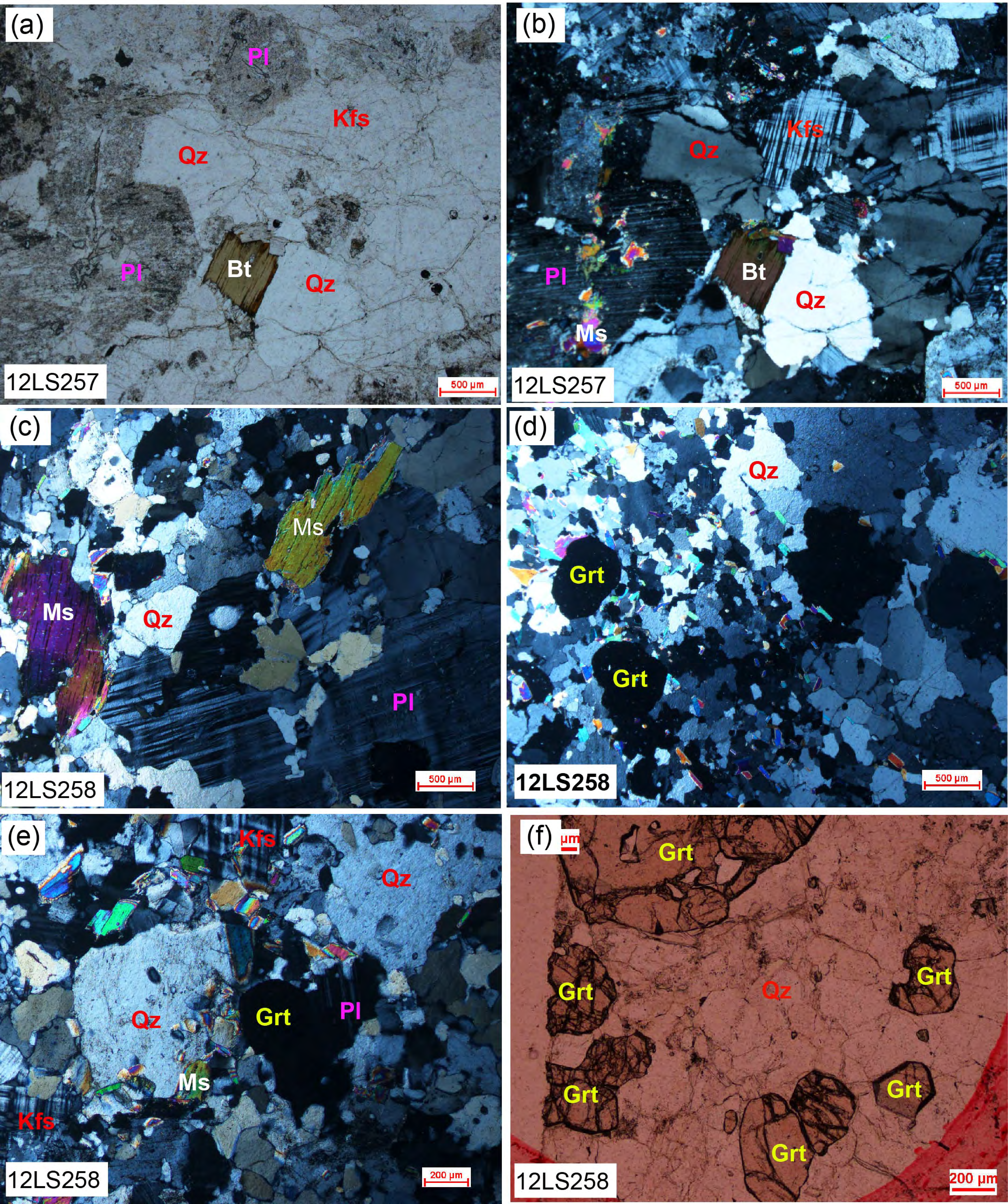
(a)
Pl
Kfs
Qz
Pl
Bt
Qz
12LS257
500 µm
(b)
Qz
Kfs
Pl
Bt
Qz
Ms
12LS257
500 µm
(c)
Ms
Ms
Qz
Pl
12LS258
500 µm
(d)
Qz
Grt
Grt
12LS258
500 µm
(e)
Kfs
Qz
Qz
Grt
Pl
Ms
Kfs
12LS258
200 µm
(f)
Grt
Grt
Qz
Grt
Grt
Grt
Grt
12LS258
200 µm

Figure 4

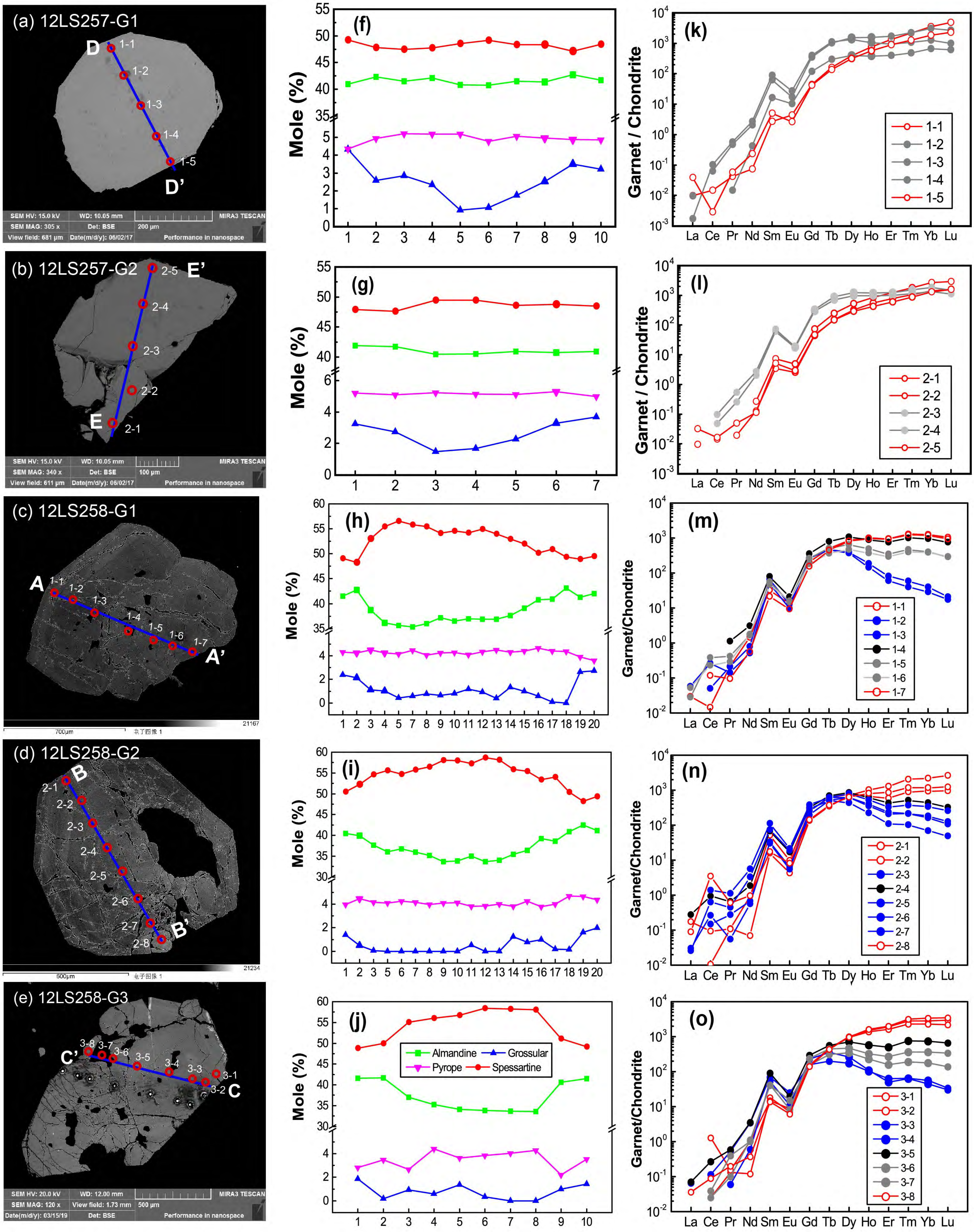

(a) 12LS257-G1
(b) 12LS257-G2
(c) 12LS258-G1
(d) 12LS258-G2
(e) 12LS258-G3
(f)
(g)
(h)
(i)
(j)
(k)
(l)
(m)
(n)
(o)
Mole (%)
Garnet / Chondrite
Garnet/Chondrite
Almandine
Grossular
Pyrope
Spessartine
La Ce Pr Nd Sm Eu Gd Tb Dy Ho Er Tm Yb Lu

Figure 5

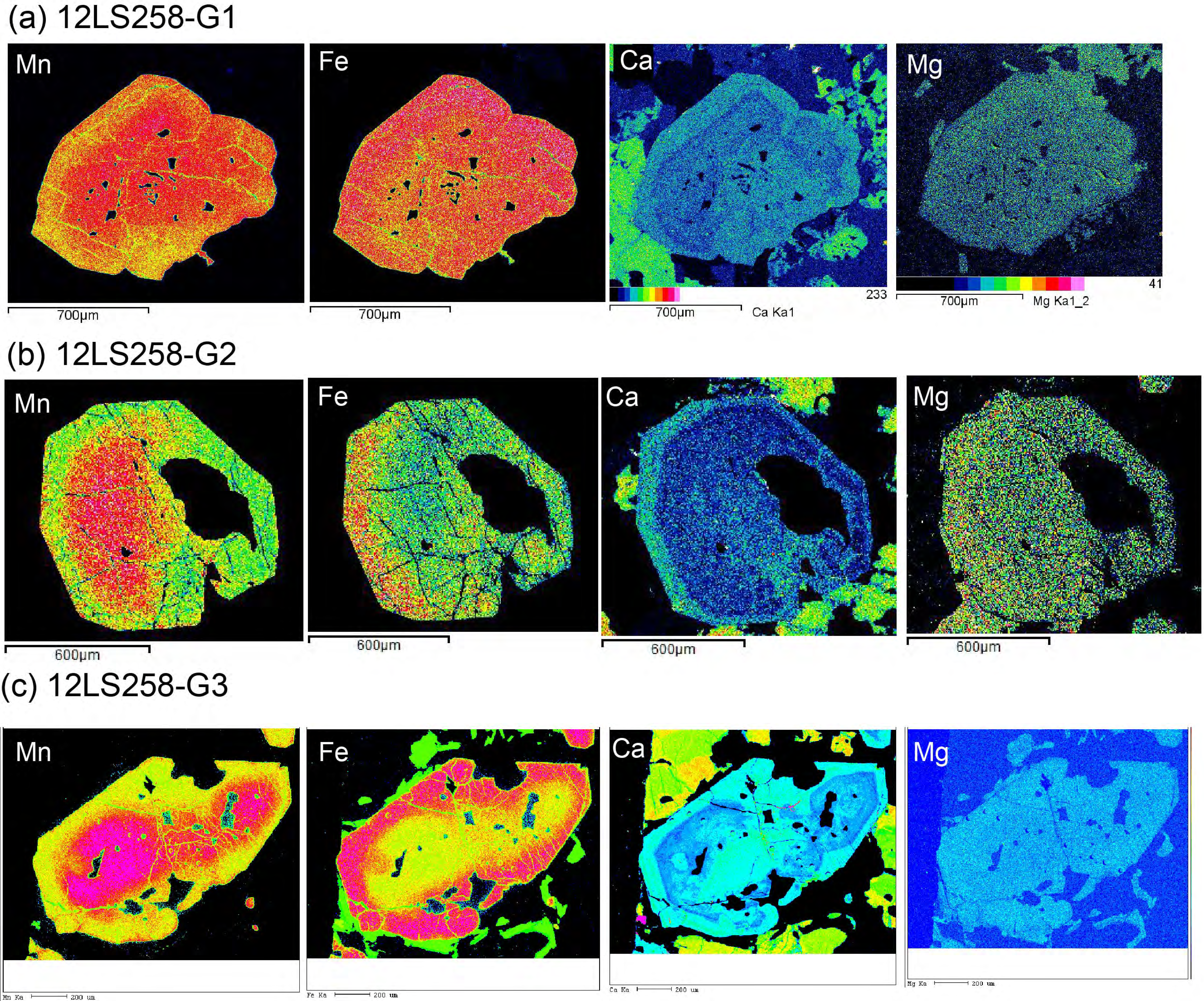
(a) 12LS258-G1
Mn
Fe
Ca
Mg
700μm
700μm
700μm
Ca Ka1
233
700μm
Mg Ka1_2
41
(b) 12LS258-G2
Mn
Fe
Ca
Mg
600μm
600μm
600μm
600μm
(c) 12LS258-G3
Mn
Fe
Ca
Mg
Mn Ka 200 um
Fe Ka 200 um
Ca Ka 200 um
Mg Ka 200 um

Figure 6

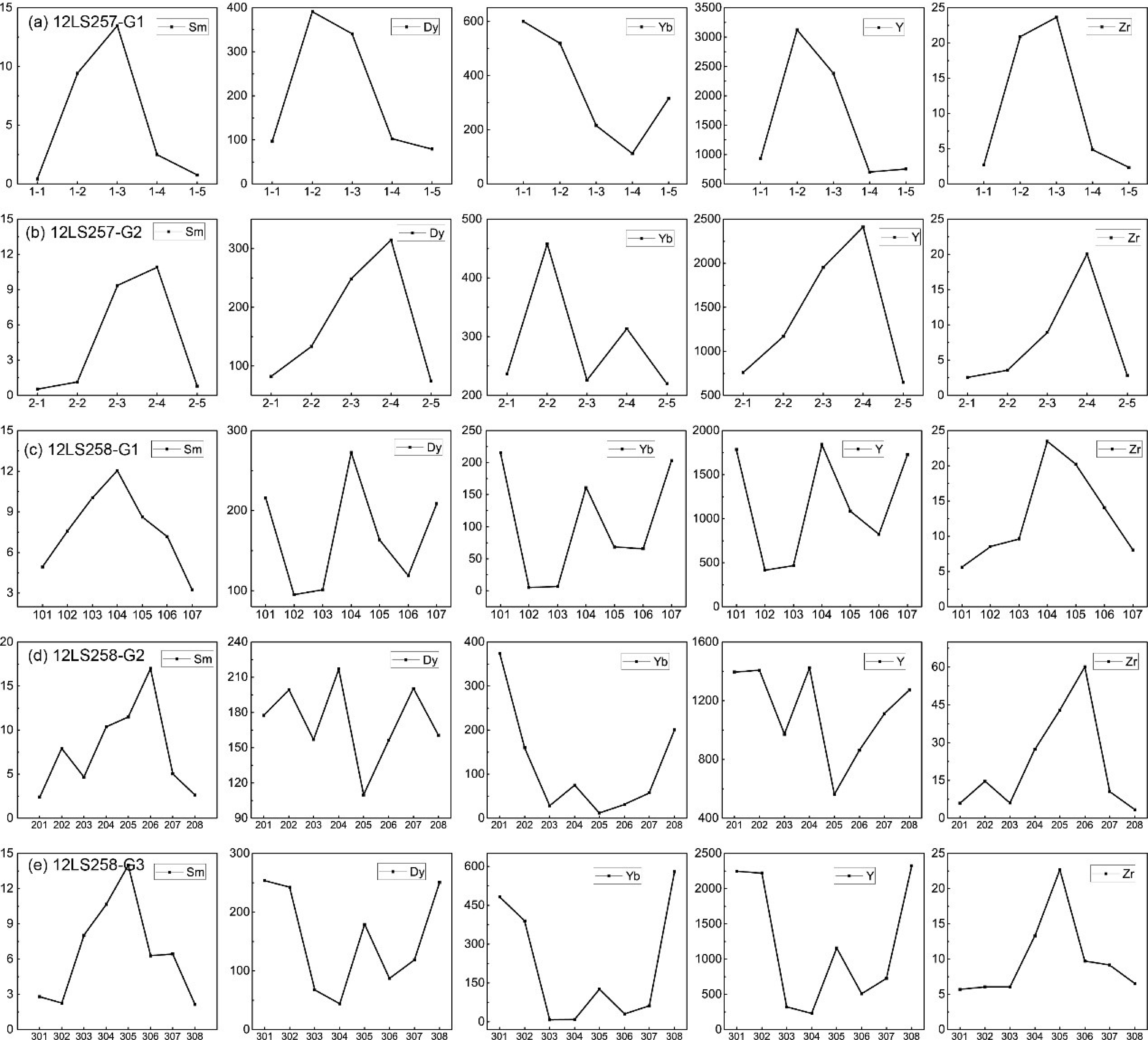

(a) 12LS257-G1
Sm
Dy
Yb
Y
Zr
1-1
1-2
1-3
1-4
1-5
(b) 12LS257-G2
2-1
2-2
2-3
2-4
2-5
(c) 12LS258-G1
101
102
103
104
105
106
107
(d) 12LS258-G2
201
202
203
204
205
206
207
208
(e) 12LS258-G3
301
302
303
304
305
306
307
308

Figure 7

(a) 12LS257 Granite
#3/80.2/6.34
#6/80.9/6.41
#5/363/9.78
#2/302/9.53
#9/78.2/6.46
#10/338/9.51
#23/133/8.63
#24/79.4/6.36
100 μm
(e) 12LS258 Pegmatite
#3/76.5/5.48
#1/76.9/5.48
#2/76.3/5.73
#4/76.2/5.26
#7/76.6/5.93
100 μm
(b) 12LS257 Granite
Intercepts at
77.4±7.9 & 302±53 Ma
MSWD = 1.4
720
560
400
240
80
207Pb/206Pb
238U/206Pb
(f) 12LS258 Pegmatite
Intercepts at
76.7 ±0.5 Ma
MSWD = 1.13
80
77
76
75
207Pb/206Pb
238U/206Pb
(c) 12LS257 Granite
Mean = 79.1 ± 0.5 Ma
MSWD = 2.1
n = 26
Number
U-Pb ages
(g) 12LS258 Pegmatite
Mean = 76.8 ± 0.4 Ma
MSWD = 0.77
n = 14
Number
U-Pb ages
(d) 12LS257 Granite
Zircon/Chondrite
(h) 12LS258 Pegmatite
Zircon/Chondrite
La Ce Pr Nd Sm Eu Gd Tb Dy Ho Er Tm Yb Lu

Figure 8

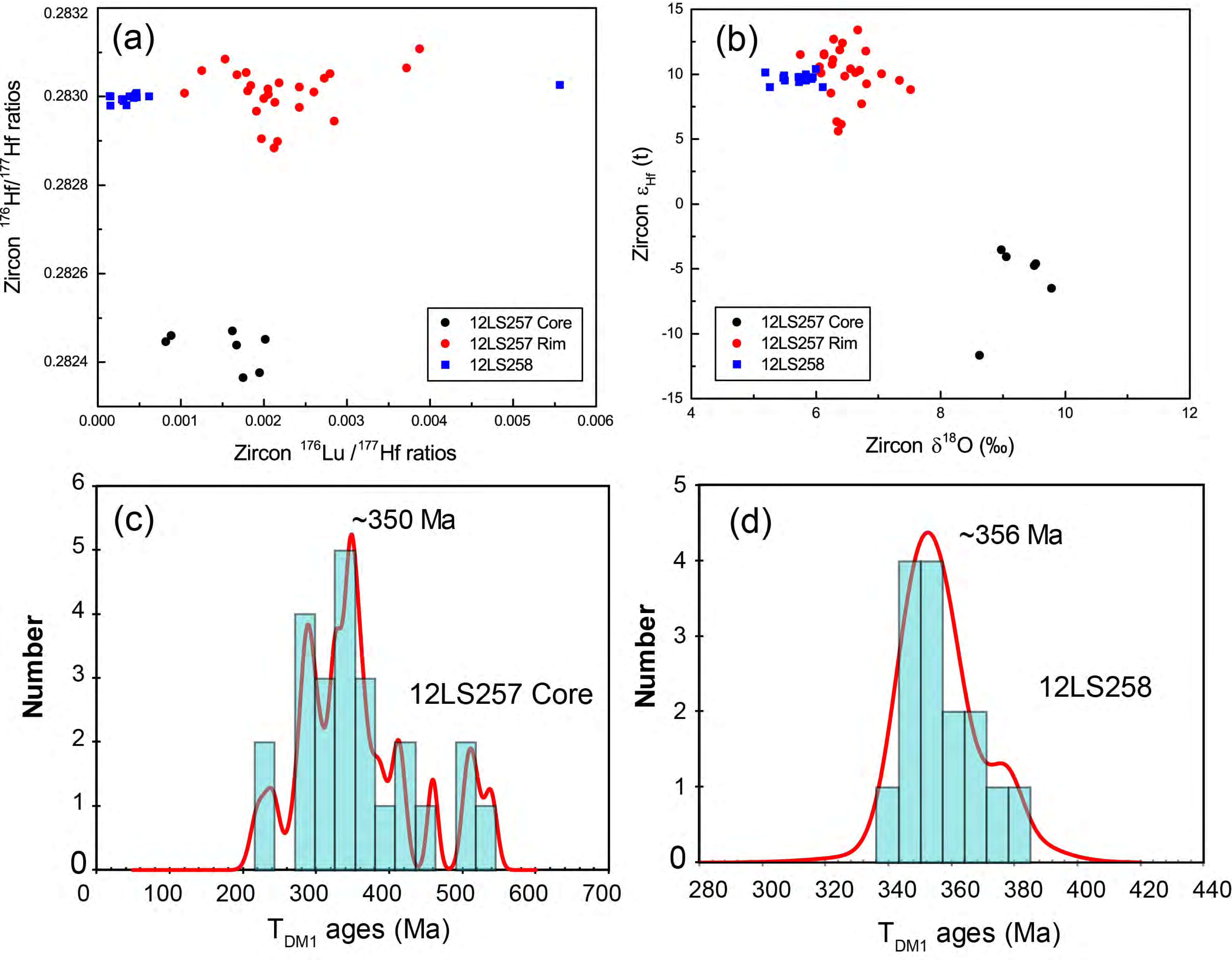

(a)
Zircon ¹⁷⁶Hf/¹⁷⁷Hf ratios
Zircon ¹⁷⁶Lu /¹⁷⁷Hf ratios
0.2824
0.2826
0.2828
0.2830
0.2832
0.000
0.001
0.002
0.003
0.004
0.005
0.006
12LS257 Core
12LS257 Rim
12LS258
(b)
Zircon εHf (t)
Zircon δ18O (‰)
15
10
5
0
-5
-10
-15
4
6
8
10
12
12LS257 Core
12LS257 Rim
12LS258
(c)
~350 Ma
12LS257 Core
Number
TDM1 ages (Ma)
0
1
2
3
4
5
6
0
100
200
300
400
500
600
700
(d)
~356 Ma
12LS258
Number
TDM1 ages (Ma)
0
1
2
3
4
5
280
300
320
340
360
380
400
420
440

Figure 9

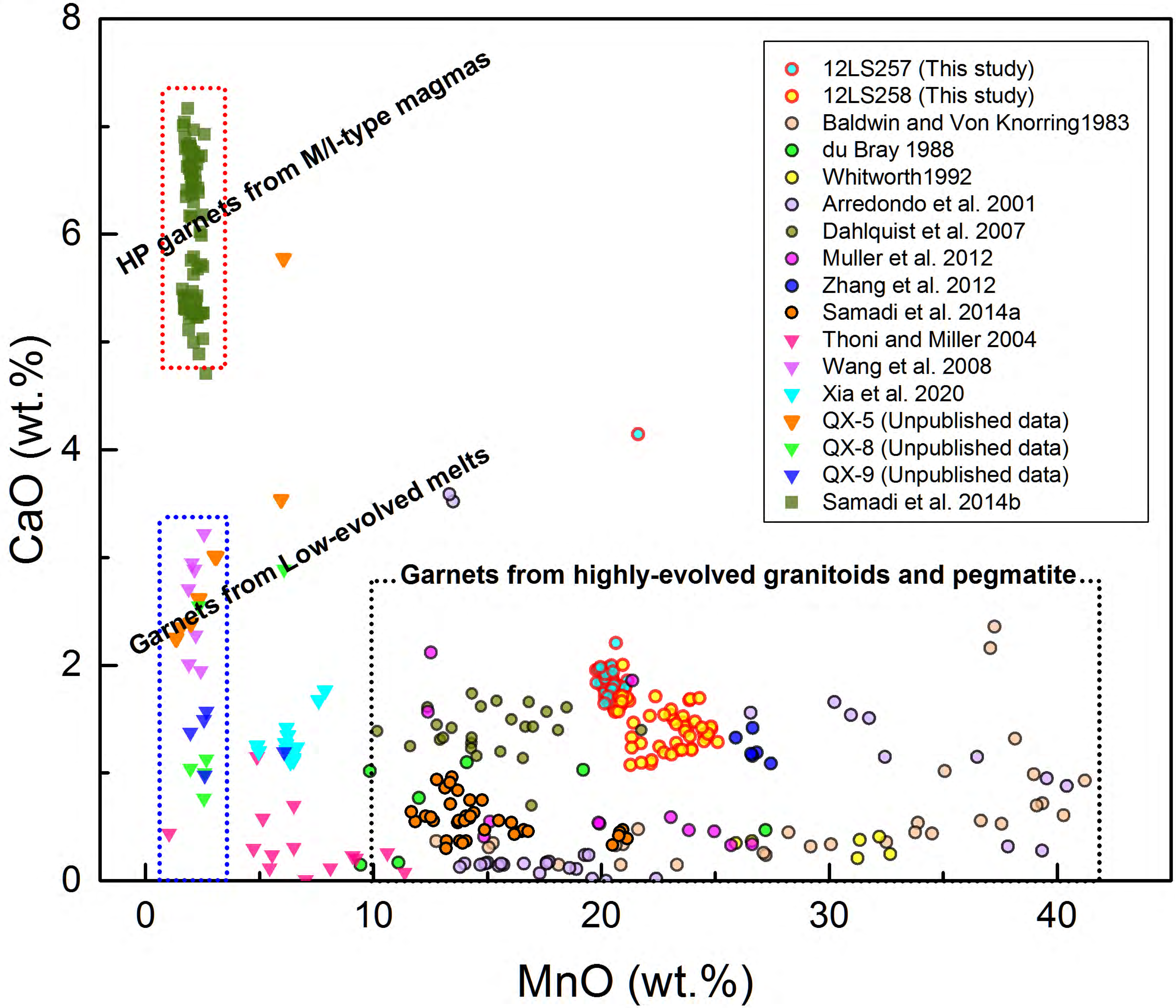

HP garnets from M/I-type magmas
Garnets from Low-evolved melts
Garnets from highly-evolved granitoids and pegmatite
12LS257 (This study)
12LS258 (This study)
Baldwin and Von Knorring1983
du Bray 1988
Whitworth1992
Arredondo et al. 2001
Dahlquist et al. 2007
Muller et al. 2012
Zhang et al. 2012
Samadi et al. 2014a
Thoni and Miller 2004
Wang et al. 2008
Xia et al. 2020
QX-5 (Unpublished data)
QX-8 (Unpublished data)
QX-9 (Unpublished data)
Samadi et al. 2014b
CaO (wt.%)
MnO (wt.%)
0
2
4
6
8
0
10
20
30
40

Figure 10


2500
2000
1500
1000
500
0
Y (ppm)
Grt-I
Grt-II
(a)
1.0
1.1
1.2
1.3
1.4
1.5
1.6
1.7
CaO (wt.%)
600
400
200
0
Yb (ppm)
G1-Core
G1-Mantle
G1-Rim
G2-Core
G2-Mantle
G2-Rim
G3-Core
G3-Mantle
G3-Rim
Grt-I
Grt-II
(b)
1.0
1.1
1.2
1.3
1.4
1.5
1.6
1.7
CaO (wt.%)